Inverse-design of high-dimensional quantum optical circuits in a complex medium

Suraj Goel
Heriot-Watt University
Saroch Leedumrongwatthanakun
Heriot-Watt University
Natalia Valencia
Heriot-Watt University https://orcid.org/0000-0003-1468-8953
Will McCutcheon
Heriot-Watt University
Claudio Conti
University of Rome
Pepijn Pinkse
University of Twente https://orcid.org/0000-0001-7912-9322
Mehul Malik (m.malik@hw.ac.uk)
Heriot-Watt University https://orcid.org/0000-0001-8395-160X

Article

Keywords:

Posted Date: May 23rd, 2022

DOI: https://doi.org/10.21203/rs.3.rs-1617041/v1

Inverse-design of high-dimensional quantum optical circuits in a complex medium

Suraj Goel,[1,*] Saroch Leedumrongwatthanakun,[1,*] Natalia Herrera Valencia,[1] Will McCutcheon,[1] Claudio Conti,[2,3,4] Pepijn W. H. Pinkse,[5] and Mehul Malik[1,†]

[1] *Institute of Photonics and Quantum Sciences, Heriot-Watt University, Edinburgh, UK*
[2] *Department of Physics, University Sapienza, Piazzale Aldo Moro 2, 00185 Rome, Italy*
[3] *Institute for Complex Systems, National Research Council (ISC-CNR), Via dei Taurini 19, 00185 Rome, Italy*
[4] *Research Center Enrico Fermi, Via Panisperna 89a, 00184 Rome, Italy*
[5] *MESA+ Institute for Nanotechnology, University of Twente, P.O. Box 217, 7500 AE Enschede, The Netherlands*

Programmable optical circuits form a key part of quantum technologies today, ranging from transceivers for quantum communication to integrated photonic chips for quantum information processing. As the size of such circuits is increased, maintaining precise control over every individual component becomes challenging, leading to a reduction in the quality of the operations performed. In parallel, minor imperfections in circuit fabrication are amplified in this regime, dramatically inhibiting their performance. Here we show how embedding an optical circuit in the higher-dimensional space of a large, ambient mode-mixer using inverse-design techniques allows us to forgo control over each individual circuit element, while retaining a high degree of programmability over the circuit. Using this approach, we implement high-dimensional linear optical circuits within a complex scattering medium consisting of a commercial multi-mode fibre placed between two controllable phase planes. We employ these circuits to manipulate high-dimensional spatial-mode entanglement in up to seven dimensions, demonstrating their application as fully programmable quantum gates. Furthermore, we show how their programmability allows us to turn the multi-mode fibre itself into a generalised multi-outcome measurement device, allowing us to both transport and certify entanglement within the transmission channel. Finally, we discuss the scalability of our approach, numerically showing how a high circuit fidelity can be achieved with a low circuit depth by harnessing the resource of a high-dimensional mode-mixer. Our work serves as an alternative yet powerful approach for realising precise control over high-dimensional quantum states of light, with clear applications in next-generation quantum communication and computing technologies.

A programmable optical circuit is an essential element for applications in fields as diverse as sensing, communication, neuromorphic computing, artificial intelligence, and quantum information processing [1–3]. The production of large, reprogrammable circuits is of paramount importance for coherently processing information encoded in light. However, there remain many challenges associated with the design, manufacture, and control of such circuits, which normally require a sophisticated mesh of interferometers constructed with bulk or integrated optics [2, 4]. Conventional construction of these circuits exploits universal programmability on two-dimensional unitary spaces to construct arbitrary high-dimensional unitary transformations [5–8], herein referred to as the "bottom-up" technique (Fig.1a). Over the past two decades, the technological development of integrated programmable circuits has enabled universal programmability in up to 20 path-encoded modes, containing a few hundreds of optical components on the same chip [9–12].

Imperfections in optical circuits such as scattering loss, unbalanced mode-mixing, and undesired cross-talk between modes are problematic as they reduce the accuracy and success probability of the implemented circuit [13–17]. These issues become increasingly challenging in large dimensions, as the number of optical elements grows quadratically with the size of the circuit [2, 4]. Such imperfections can be addressed to some extent by increasing the depth of the circuit through the introduction of additional phase shifters and beamsplitters [13–15, 18, 19]. However, these additional components necessitate additional control, further increasing the demands associated with circuit complexity. In this work, we present an alternative solution where the optical circuit is embedded in a higher-dimensional space of a large ambient mode-mixer such as a random scattering medium, placed between reprogrammable phase planes (Fig.1b). This "top-down" approach harnesses the complicated scattering process within a large mode-mixer to forgo control over each individual circuit element. Instead, an inverse-design approach is used that employs algorithmic techniques to program an optical circuit with a desired functionality within the random scattering medium [20, 21]. Similar approaches based on inverse-design have been used in multi-plane light converters (MPLC) for spatial-mode manipulation [22–24], where free-space propagation is commonly used in place of a random scattering medium (Fig.1c). Furthermore, inverse-design techniques have also enabled a variety of optical circuits tailored towards specific functionalities, ranging from designs of on-chip photonic devices [25] to arrangements of bulk optical elements for fundamental quantum experiments [26–29].

The capability to manipulate quantum states of light using large-scale programmable circuits promises a myr-

* These authors contributed equally to this work
† Email address: m.malik@hw.ac.uk; Website: http://bbqlab.org

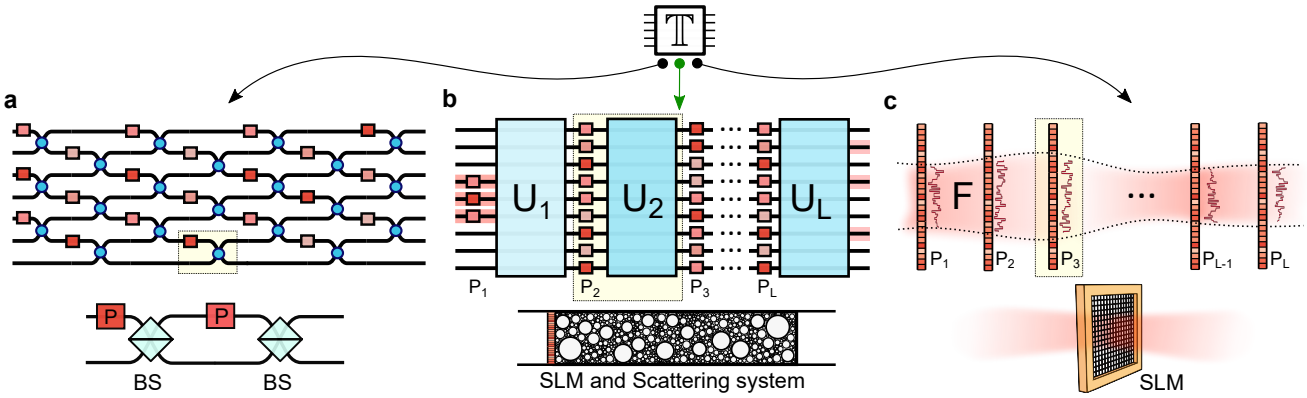

Figure 1. **Designing programmable optical circuits:** A general linear transformation $\mathbb{T}$ can be implemented via (a) the conventional "bottom-up" approach, where the circuit is constructed from units consisting of beamsplitters (BS) and phase shifters (P), or (b) the herein proposed "top-down" approach, where a target d-dimensional linear circuit is implemented within a large ambient mode-mixer with dimension $n > d$, where $n - d$ auxiliary modes serve as an additional resource. The technique harnesses random unitaries U_j (such as a complex scattering system) interspersed with controllable phase planes P_j implemented via spatial light modulators (SLMs), which provide programmability over the target circuit. A similar approach is used in (c) multi-plane light converters, where the random unitaries are replaced with free-space propagation F.

iad of applications in quantum information science, ranging from the demonstration of computational advantage [30] to the realisation of quantum networks [31]. In this regard, high-dimensional quantum systems offer significant advantages in terms of increased information capacity and noise-resistance in quantum communication [32–34], while also enabling more practical tests of quantum nonlocality [35, 36]. While methods for the transport [37, 38] and certification [39–41] of high-dimensional entanglement have seen rapid progress over the past few years, scalable techniques for its precise manipulation and measurement are still lacking. As an alternative to the bottom-up approach normally implemented on integrated platforms [10], inverse-design techniques have been used for realising quantum gates in dimensions up to $d = 4$ using bulk optical interferometers [42, 43] and in $d = 5$ with multi-plane light conversion [44, 45]. In parallel, recent advances in control over light scattering in complex media [46, 47] have enabled linear optical circuits for classical light [48, 49] and demonstrations of programmable two-photon quantum interference [50–52], showing their clear potential to serve as a high-dimensional quantum photonics platform.

In this article, we harness light scattering through an off-the-shelf multi-mode fibre to program generalised quantum circuits for transverse spatial photonic modes in dimensions up to seven. We apply these circuits for the manipulation of high-dimensional entangled states of light in multiple spatial-mode bases, demonstrating high-dimensional Pauli-$\mathbb{Z}$ and $\mathbb{X}$ gates, discrete Fourier transforms, and random unitaries in the macro-pixel and OAM spatial-mode bases [41, 53]. Furthermore, in contrast with single-outcome projective measurements that are inherently inefficient [54], our technique realises generalised transformations to a spatially localised "pixel" basis, effectively turning the channel itself into a generalised multi-outcome measurement device. By harnessing this functionality, we show how the on-demand programmability of our gates enables us to both transport and certify entanglement within the same complex medium. Such multi-outcome measurements can be easily integrated with next-generation single-photon-detector arrays [55] and provide a key functionality in many quantum information applications, such as allowing one to overcome fair-sampling assumptions [56].

I. Top-Down Programmable Circuits: Concept and Experimental Implementation

An optical circuit is described by a linear transformation $\mathbb{T}$ that maps a set of input optical modes onto a set of output modes [57, 58]. The linear circuit $\mathbb{T}$ of dimension d is built from a cascade of optical mode mixers U, and phase shifters P. A deterministic construction can be based on a cascade of reconfigurable Mach–Zehnder interferometers, wherein U_j represents the embedded balanced two-mode mixer, i.e. a 50:50 beam splitter, and the P_j are phase shifters (Fig.1a) [5, 7]. As an alternative to this deterministic *bottom-up* construction, the *top-down* design presented here relies on the capability to harness large, complex, inter-modal mode mixers U_j of dimension n ($U_j \in \mathcal{U}(\mathbf{n})$) and reconfigurable phase planes $P_j = \mathrm{diag}(e^{i\boldsymbol{\theta}})$ to construct a programmable target circuit $\mathbb{T}$ of a smaller size ($d \leqslant n$) embedded within the larger mode-mixers (Fig.1b). The decomposition of a top-down programmable circuit is represented as

$$\mathbf{T} \approx \prod_{j=1}^{L \leqslant \mathcal{O}(\mathbf{d})} U_j P_j, \tag{1}$$

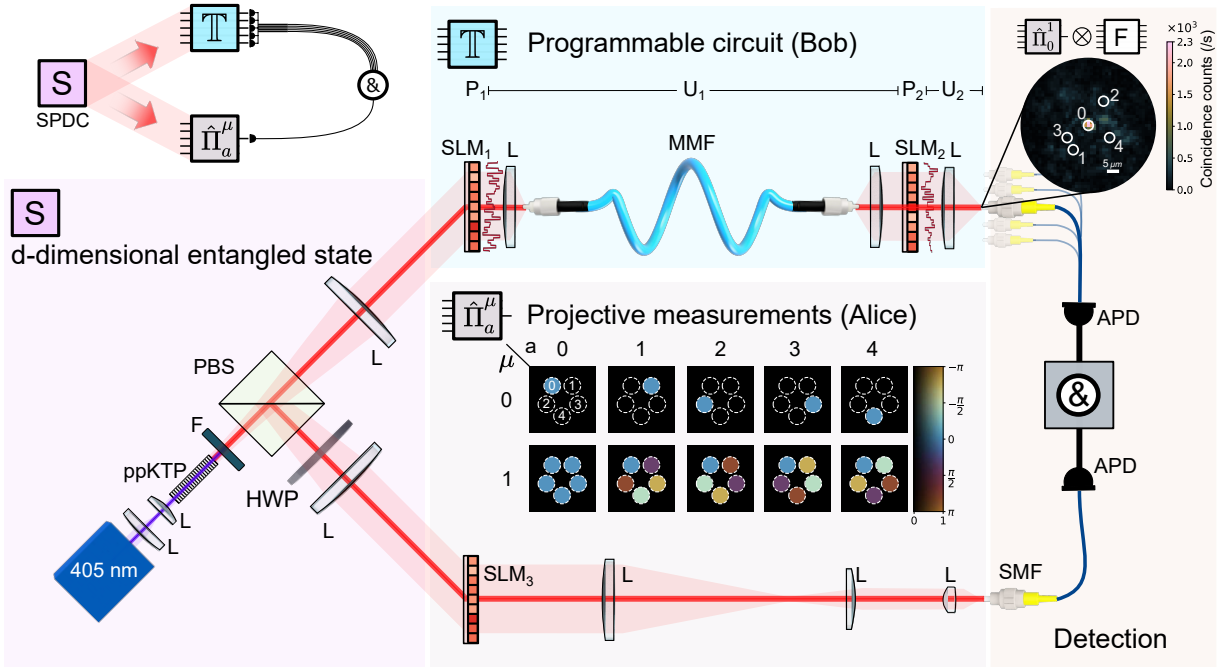

Figure 2. **Experimental setup**: A high-dimensional spatially entangled two-photon state is generated via Type-II spontaneous parametric downconversion (SPDC) in a periodically poled Potassium Titanyl Phosphate (ppKTP) crystal. The two photons are spatially separated by a polarising beamsplitter (PBS) and sent to two parties, Alice and Bob. Alice performs single-outcome projective measurements $\hat{\Pi}_a^\mu$ that measure whether a photon is carrying spatial mode a from modal basis μ. These are performed by a combination of a spatial light modulator (SLM_3), single-mode fibre (SMF), and a single-photon avalanche photodiode (APD). Bob implements a top-down programmable circuit that is constructed from a multi-mode optical fibre (MMF) placed between two programmable spatial light modulators ($SLM_{1,2}$). The circuit is used to program a variety of high-dimensional quantum gates and serves as a generalised multi-outcome device. (Circular insert) A coincidence image depicting a five-outcome measurement in basis $\mu = 1$ performed with the Fourier $\mathbb{F}$ gate at Bob. The image is obtained by scanning a detector across the output of the circuit, conditioned on a measurement of $\hat{\Pi}_{a=0}^{\mu=1}$ at Alice, and shows a large intensity in mode 0 due to strong spatial-mode correlations. Coincidence detection events between Alice and Bob are registered by time-tagging electronics. (L: lens, F: filter, HWP: half-wave plate)

where L is the depth of the circuit (the number of layers), and the target circuit $\mathbb{T}$ is embedded in the total transfer matrix of the system $\mathbf{T}$. Optimal choices for the large mode-mixer dimension (n) and the circuit depth (L) for a given target circuit dimension (d) are discussed in Section III.

We experimentally construct the programmable optical circuit with a 2-metre-long multi-mode fibre (MMF) positioned between two programmable phase planes, P_1 and P_2, implemented on spatial light modulators (SLMs) as depicted in Fig. 2. The MMF serves as a large, complex mode-mixer with dimension $n \approx 200$ that provides complicated inter-modal coupling [59–61], while the SLMs provide programmability over the circuit to be implemented. The circuit can be decomposed as $\mathbf{T} = U_2 P_2 U_1 P_1$, where U_1 represents the transfer matrix of the optical system consisting of the MMF and the associated coupling optics and U_2 is the $2f$ lens system. To construct the circuit, we begin by characterising U_1 in a referenceless manner via our developed technique. Random phase patterns are displayed on the planes P_1 and P_2 and the resulting intensity speckle images are measured at the output. The data set is then used to optimise the machine learning model that describes the optical system of our experiment using the gradient descent method (see Supplementary Information S.2). Once we have complete knowledge of the mode-mixer U_1, a given target circuit is then programmed using a solution of phase patterns obtained from the wavefront-matching (WFM) algorithm [25, 62, 63]. The WFM algorithm is an inverse-design technique that calculates the reconfigurable phase planes by iterating though each of them in order to maximise the overlap between a set of input fields with the desired output ones, and repeating this procedure several times (see Supplementary Information S.5 for details).

II. Applications of Quantum Gates: Manipulation and Certification of High-Dimensional Entanglement

We utilise the programmable circuit to manipulate spatially entangled two-photon states in a range of dimensions, $d \in \{2, 3, 5, 7\}$ (see S.1 for details of the generated

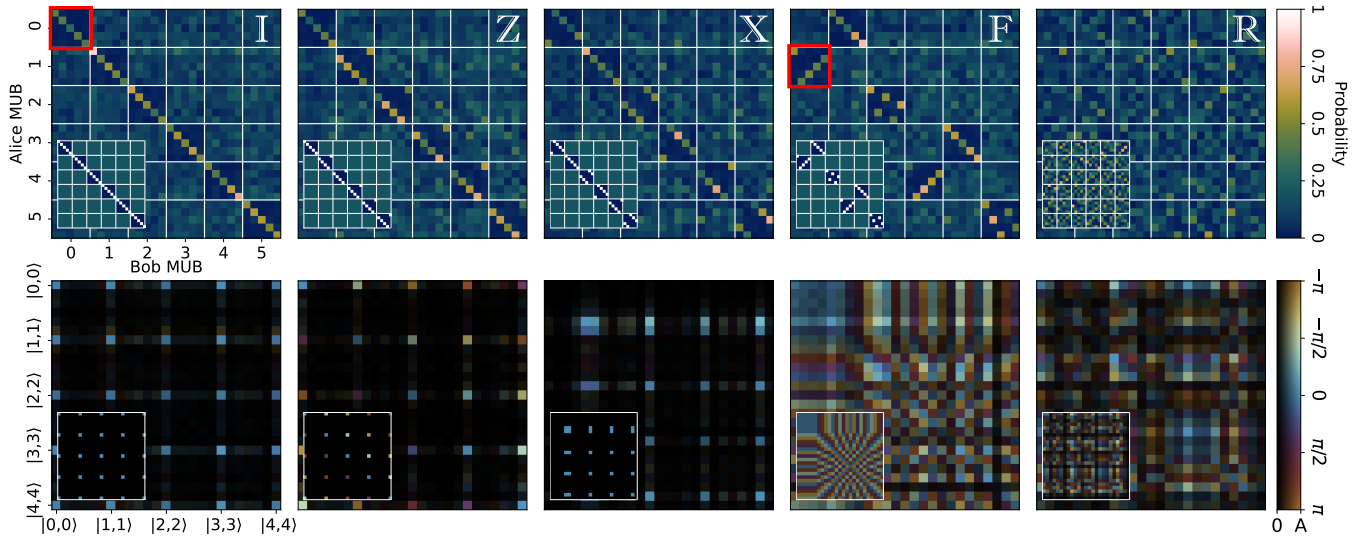

Figure 3. **Manipulation and certification of high-dimensional entanglement**: Normalised two-photon coincidence counts (top row) and reconstructed density matrices (bottom row) corresponding to the output state obtained after local operation of the Identity $\mathbb{I}$, Pauli-$\mathbb{Z}$, Pauli-$\mathbb{X}$, Fourier $\mathbb{F}$, and random unitary $\mathbb{R}$ gates on an input two-photon, five-dimensional entangled state in the macro-pixel basis. The two-photon coincidences are measured in all six mutually unbiased bases (MUBs $\mu \in \{0...5\}$) via projective measurements at Alice and Bob. Due to state-channel duality, tomography of the output two-photon state is equivalent to performing ancilla-assisted process tomography of the gates themselves [37, 64]. The fidelities of the reconstructed density matrices are reported in Table I. The Identity and Fourier gates enable our circuit to be used as a multi-outcome measurement device in MUBs $\mu \in \{0, 1\}$ (red squares). By applying a two-basis entanglement witness on these data [39], we are able to certify four-dimensional entanglement using the channel itself as a measurement device.

states). As shown in Fig. 2, the two photons are generated via the process of spontaneous parametric down-conversion (SPDC) and sent to two parties, Alice and Bob. Bob's photon is locally manipulated by the programmable circuit $\mathbb{T}$, while Alice's photon is detected via single-outcome projective measurements $\hat{\Pi}_a^\mu$. These measurements project the photon in a particular mode a in basis μ via the combination of a holographic spatial light modulator (SLM_3) and single mode fibre [54, 65]. These *single-outcome measurements* require one to perform d projections to realise a complete measurement, giving them a maximum effective efficiency of $1/d$, which is normally lower due to loss. In contrast, our programmable circuit $\mathbb{T}$ performs generalised basis transformations to a localised "pixel" basis with a maximum theoretical efficiency of unity (see Section III), enabling *multi-outcome measurements* in any given basis. The circuit is programmed to operate on two different input bases, the macro-pixel basis [41] and the orbital-angular-momentum (OAM) basis [53], while the target output modes are randomly selected from the set of all possible foci at the output of the circuit. We then implement a variety of different target gates including the identity-$\mathbb{I}$, Pauli-$\mathbb{Z}$, Pauli-$\mathbb{X}$, Fourier-$\mathbb{F}$, and random unitaries-$\mathbb{R}$ by programming the circuit using the wavefront-matching algorithm.

In order to verify that these gates preserve quantum coherence, we apply them on the input high-dimensionally entangled states and reconstruct the resulting output state via quantum state tomography (S.4). Due to state-channel duality, tomography of the output two-photon state is equivalent to performing ancilla-assisted process tomography of the gates themselves [37, 64]. In this manner, we can quantify how close to ideal these gates are, while also verifying that they preserve high-dimensional entanglement. To showcase the versatility of our platform, we program 296 instances of all gates, sampling from different output foci in different dimensions and input bases. Fig. 3 (top row) shows examples of normalised two-photon coincidence count data in all mutually unbiased bases (MUBs) for five-dimensional $\mathbb{I}$, $\mathbb{Z}$, $\mathbb{X}$, $\mathbb{F}$, and $\mathbb{R}$ gates programmed for the macro-pixel basis. Fig. 3 (bottom row) shows density matrices of the manipulated two-photon states reconstructed from these data, presenting a clear agreement with theoretical prediction (insets). This can be quantified via their fidelity (S.6) to the ideal output states, which is reported in Table I for all dimensions in the macro-pixel basis. Our fidelity calculation takes into account the non-maximally entangled nature of the input entangled state. Results for gates implemented in the LG basis are presented in S.7. It is noteworthy that the five-dimensional reconstructed state after the identity gate $\mathbb{I}$ has a fidelity of $\mathcal{F}(\rho_o, |\Phi^+\rangle\langle\Phi^+|) = 83.8 \pm 1.5\%$ to the maximally entangled state, which exceeds the bound necessary to certify five-dimensional entanglement.

While we have verified that these gates are able to manipulate and preserve high-dimensional entanglement, we now demonstrate how they can be used for the certifica-

tion of entanglement using the channel itself. Entanglement certification requires correlation measurements in at least two MUBs [39], which are normally performed with SLM-based projective single-outcome measurements (as done at Alice). Our programmable circuit functions as a generalised multi-outcome measurement device, allowing measurements to be made both in the pixel basis $\mu = 0$ (via the identity gate $\mathbb{I}$), as well as the first MUB $\mu = 1$ (via the Fourier gate $\mathbb{F}$) with an appropriate single-photon detector array. An example of the five-outcome MUB measurement is shown in Fig. 2 (insert) that depicts the output of the $\mathbb{F}$ gate, conditioned on a MUB measurement $\hat{\Pi}_{a=0}^{\mu=1}$ at Alice. The image is obtained by tilting wavefronts using SLM_2, which is equivalent to scanning a detector across the output (as shown in the illustration). The increased coincidence counts observed in mode 0 are due to the strong two-photon spatial-mode correlations exhibited by the entangled state. The coincidence count data corresponding to a two-basis measurement obtained by programming the circuit in this manner are highlighted in Fig. 3 (red squares). Using these data, we obtain a fidelity of $68.9 \pm 3.2\%$ to a five-dimensional maximally entangled state, certifying the presence of four-dimensional entanglement. In this manner, the multi-mode optical fibre can be used to both *transport* as well as *certify* high-dimensional entanglement. It is important to note that while we have used two MUBs for entanglement certification, the programmability of our circuit in general allows for measurements in multiple or even "tilted" MUBs [39], which would lead to increased fidelities and robustness to noise.

The coincidence image in Fig. 2 also provides information about scattering loss outside the output modes of interest. This allows us to measure the success probability of the gate operation, which is defined as the ratio of coincidence counts in the target output modes over the total coincidence counts integrated over all outputs in one polarisation channel. We perform this measurement on three randomly chosen implementations of the $\mathbb{F}$ gates in $2, 3$ and 5 dimensions and measure a success probability of 0.36 ± 0.01, 0.27 ± 0.03, and 0.18 ± 0.04, respectively. Additional information about the success probability and optical transmittance of the device is provided in S.6. It is worth noting that for this proof-of-concept demonstration, we only control a single polarisation channel of the multi-mode fibre, thus reducing the success probability by about half. Controlling both polarisation channels of the multi-mode fibre can increase the success probability by almost a factor two as well as improve the fidelity of the implemented circuits. In addition, the results in Table I report the circuits with the highest achieved fidelities. While in theory using random-unitary as a mode-mixer, this is statistically expected to be the same for all types of implemented circuits at a given dimension, experimental imperfections in the characterisation and properties of U_1 result in a spread of fidelities with a lower average (please see Supplementary Information S.7 for details).

Table I: Quantum process fidelities of inverse-designed gates in the macro-pixel basis. Due to state-channel duality, these are equivalent to the fidelities of the two-photon entangled states manipulated by these gates.

Gate	$d = 2$	$d = 3$	$d = 5$	$d = 7$
$\mathbb{I}$	$97.3 \pm 0.3\%$	$94.4 \pm 0.2\%$	$84.7 \pm 0.4\%$	$73.1 \pm 0.4\%$
$\mathbb{Z}$	$97.7 \pm 0.4\%$	$93.5 \pm 0.3\%$	$77.7 \pm 0.4\%$	$61.4 \pm 0.4\%$
$\mathbb{X}$	$97.1 \pm 0.4\%$	$92.6 \pm 0.2\%$	$78.8 \pm 0.5\%$	$58.8 \pm 0.5\%$
$\mathbb{F}$	$96.0 \pm 0.6\%$	$89.4 \pm 0.4\%$	$75.9 \pm 0.4\%$	$57.5 \pm 0.4\%$
$\mathbb{R}$	$96.5 \pm 0.5\%$	$90.2 \pm 0.2\%$	$81.1 \pm 0.4\%$	$63.6 \pm 0.4\%$

III. Programmability and Scalability

We have successfully demonstrated the ability to perform various gates in multiple spatial-mode bases in dimensions $2, 3, 5$ and 7. However, as the dimension of the target gate increases, maintaining high fidelities and success probabilities becomes increasingly challenging. It is thus imperative to examine the programmability and scalablility of our design and address ways to improve its performance and target practical experimental regimes to work in. We investigate these numerically by implementing a circuit based on Eq. 1 and varying three major design parameters—the dimension of the mode mixers, n, the dimension of the target gate, d, and the depth of the circuit, L. Multiple implementations of the $\mathbb{I}$, $\mathbb{X}$, $\mathbb{Z}$, $\mathbb{F}$, and $\mathbb{R}$ gates are simulated for specific values of the design parameters by changing the random-unitary mode mixers and the sets of input and output modes for each instance. For each gate, we calculate the fidelity with respect to the ideal target gate and the success probability.

The key design considerations we address are: what dimension of mode mixers (n) should be chosen? And how many layers (L) is it practical to use, given the optical losses usually present at interfaces, and the experimental overhead involved? Figs. 4a-d depict simulation results showing how the fidelity and success probability of the top-down design ($n > d$) scale as a function of either the dimension of mode mixers (n) or the depth of circuit (L), while keeping other design parameters constant. The first observation is that increasing the size of the mode mixers (n) increases the circuit fidelity (Fig. 4a). This demonstrates that even when implementing practical low depth circuits, such as we have presented here, high fidelities can be reached, with high-dimensional mode mixers serving as a key resource for this behaviour. Furthermore, for $d/n < 0.1$ the success probability is approximately constant with n (Fig. 4b), allowing high-dimensional mode mixers to be employed without affecting the success probability.

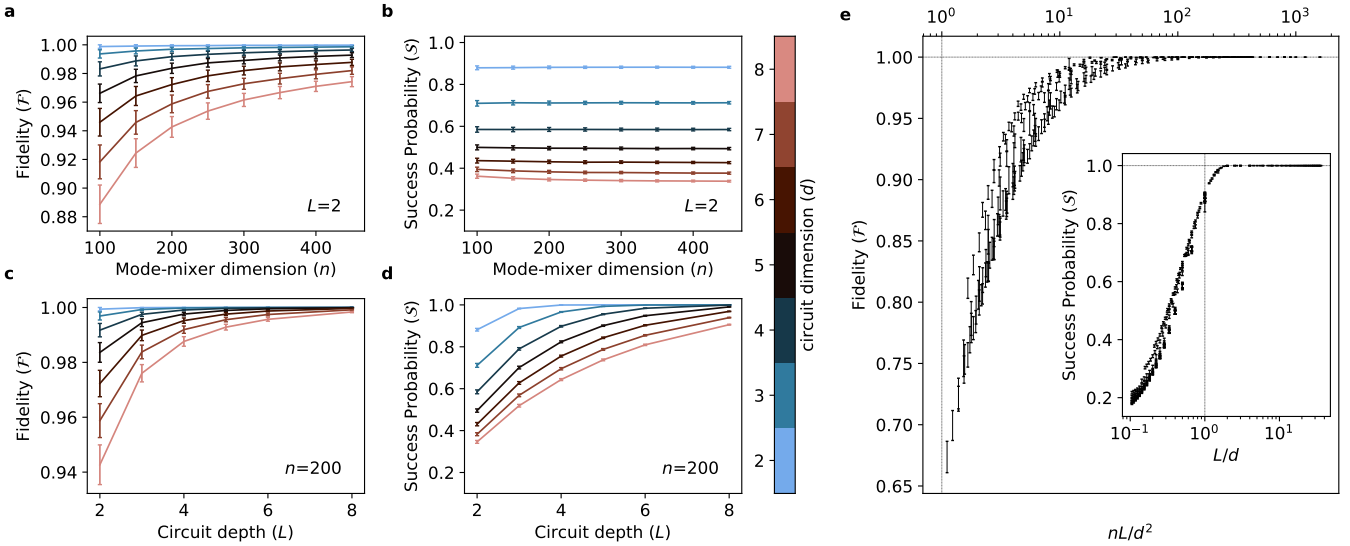

Figure 4. **Programmability and Scalability of top-down optical circuits**: (a-b) Fidelity ($\mathcal{F}$) and success probability ($\mathcal{S}$) of a d-dimensional quantum optical circuit as a function of the dimension of mode-mixers (n) for a circuit depth of $L = 2$. (c-d) $\mathcal{F}$ and $\mathcal{S}$ as a function of L for $n = 200$. (e) A plot of Fidelity versus the parameter nL/d^2 in the regime where $d/n < 0.1$. The plot shows a converging trend towards unit Fidelity ($\mathcal{F} = 1$), demonstrating that full programmability can be achieved by increasing either the mode-mixer dimension n or the circuit depth L. (Insert) A plot of Success probability versus the parameter L/d shows convergence to unity when the number of phase planes approaches $L \approx \mathcal{O}(d)$.

Alongside this, we observe that increasing the depth of the circuit (L) increases both fidelity and success probability (Figs. 4c-d), generalising recent results into the $n > d$ regime [66, 67]. In practise, however, scaling up the circuit depth introduces experimental overheads in the form of propagation and interface losses and accumulation of errors. In general, we observe that the fidelity increases and converges to unity (Fig. 4e for $d/n < 0.1$) when the total number of reconfigurable elements nL exceeds the requirement for parameterising a d-dimensional unitary transform $\mathcal{O}(d^2)$, thereby showing a high level of programmability of the top-down design. Furthermore, the convergence of the success probability to unity occurs when the circuit depth is on the order of the circuit dimension $L \approx \mathcal{O}(d)$. This is because there are $d(n-d)$ amplitudes in the transformation which correspond to scattering from the target input modes, to modes outside of the target output modes, and to achieve unit success probability these must all vanish requiring at least this many controllable parameters. The top-down approach thus presents a powerful route towards realising high-fidelity circuits by harnessing the resource of a high-dimensional mode-mixing space ($n > d$), while operating in a practical, low circuit depth regime ($L \leqslant \mathcal{O}(d)$). Full details of these simulations are presented in Supplementary Information S.8.

IV. Conclusion and Outlook

We have demonstrated that programmable optical circuits in the transverse-spatial domain can be reliably implemented using the top-down approach that incorporates complex scattering processes between reconfigurable phase planes. Using our technique, we programmed high-dimensional quantum gates within a multi-mode fibre and used them to manipulate high-dimensional entangled states of light in two different spatial-mode bases. We verified that these gates preserve quantum coherence by certifying that high-dimensional entanglement persists after gate operations. We demonstrated how our gates function as a generalised multi-outcome measurement device, enabling the MMF channel to both transport, manipulate, and certify high-dimensional entanglement. Finally, we performed extensive numerical investigations studying the scalability of our approach, concluding that high circuit fidelities can be reached by harnessing the resource of a high-dimensional mode-mixer, while staying within the practical regime of low circuit depth. Fundamental aspects of circuit design still present important open challenges, such as proving that the technique can be used for the universal implementation of unitary transformations, deterministic calculations for setting phase shifters, and optimising these circuits for better performance.

Beyond the transverse spatial degree-of-freedom, our methods readily generalise to other platforms where phase shifters and mode-mixers can be realised. For instance, implementations of top-down designs in in-

tegrated optics will be forthcoming as random-mixed waveguides develop and low-loss reconfigurable phase shifters become available [68–70]. Further developments must also address practical issues including modal dispersion and spatio-temporal mixing that are present in long multi-mode fibres and thick scattering media. These obstacles, however, enable the extension of the top-down circuit design into the spectral-temporal domain [71–74]. By demonstrating the practical realisation of high-dimensional programmable optical circuits—within the transmission channel itself—our work overcomes a significant hurdle facing the adoption of high-dimensional encoding in quantum communication systems, and paves the way for practical implementations of programmable optical circuits in various near-term photonic and quantum technologies including sensing and computation.

Acknowledgments

This work was made possible by financial support from the QuantERA ERA-NET Co-fund (FWF Project I3773-N36), the UK Engineering and Physical Sciences Research Council (EPSRC) (EP/P024114/1) and the European Research Council (ERC) Starting grant PIQUaNT (950402). Colormaps for all the figures in this article are adopted from [75].

[1] Bhavin J Shastri, Alexander N Tait, T. Ferreira de Lima, Wolfram H P Pernice, Harish Bhaskaran, C D Wright, and Paul R Prucnal, *Photonics for artificial intelligence and neuromorphic computing,* Nature Photonics **15**, 102 (2021).

[2] Wim Bogaerts, Daniel Pérez, José Capmany, David A B Miller, Joyce Poon, Dirk Englund, Francesco Morichetti, and Andrea Melloni, *Programmable photonic circuits,* Nature **586**, 207 (2020).

[3] Gordon Wetzstein, Aydogan Ozcan, Sylvain Gigan, Shanhui Fan, Dirk Englund, Marin Soljačić, Cornelia Denz, David A B Miller, and Demetri Psaltis, *Inference in artificial intelligence with deep optics and photonics,* Nature **588**, 39 (2020).

[4] Nicholas C. Harris, Jacques Carolan, Darius Bunandar, Mihika Prabhu, Michael Hochberg, Tom Baehr-Jones, Michael L. Fanto, A. Matthew Smith, Christopher C. Tison, Paul M. Alsing, and Dirk Englund, *Linear programmable nanophotonic processors,* Optica **5**, 1623 (2018).

[5] Michael Reck, Anton Zeilinger, Herbert J Bernstein, and Philip Bertani, *Experimental realization of any discrete unitary operator,* Physical Review Letters **73**, 58 (1994).

[6] David A B Miller, *How complicated must an optical component be?* Journal of the Optical Society of America A **30**, 238 (2013).

[7] William R. Clements, Peter C. Humphreys, Benjamin J. Metcalf, W. Steven Kolthammer, Ian A. Walsmley, and Ian A. Walmsley, *Optimal design for universal multiport interferometers,* Optica **3**, 1 (2016), arXiv:1603.08788.

[8] Shreya P Kumar and Ish Dhand, *Unitary matrix decompositions for optimal and modular linear optics architectures,* Journal of Physics A: Mathematical and Theoretical **54**, 045301 (2021).

[9] Jacques Carolan, Christopher Harrold, Chris Sparrow, E. Martin-Lopez, Nicholas J. Russell, Joshua W. Silverstone, Peter J. Shadbolt, Nobuyuki Matsuda, Manabu Oguma, Mikitaka Itoh, Graham D. Marshall, Mark G. Thompson, Jonathan C.F. F. Matthews, Toshikazu Hashimoto, Jeremy L. O'Brien, and Anthony Laing, *Universal linear optics,* Science **349**, 711 (2015), arXiv:1505.01182.

[10] Jianwei Wang, Fabio Sciarrino, Anthony Laing, and Mark G Thompson, *Integrated photonic quantum technologies,* Nature Photonics **14**, 273 (2020).

[11] Rui Tang, Ryota Tanomura, Takuo Tanemura, and Yoshiaki Nakano, *Ten-Port Unitary Optical Processor on a Silicon Photonic Chip,* ACS Photonics (2021), 10.1021/acsphotonics.1c00419.

[12] Caterina Taballione, Malaquias Correa Anguita, Michiel de Goede, Pim Venderbosch, Ben Kassenberg, Henk Snijders, Devin Smith, Jörn P Epping, Reinier van der Meer, Pepijn WH Pinkse, *et al.*, *20-mode universal quantum photonic processor,* (2022), arXiv:2203.01801.

[13] David A. B. Miller, *Perfect optics with imperfect components,* Optica **2**, 747 (2015).

[14] Roel Burgwal, William R. Clements, Devin H. Smith, James C. Gates, W. Steven Kolthammer, Jelmer J. Renema, and Ian A. Walmsley, *Using an imperfect photonic network to implement random unitaries,* Optics Express **25**, 28236 (2017), arXiv:1612.01199.

[15] Sunil Pai, Ben Bartlett, Olav Solgaard, and David A. B. Miller, *Matrix optimization on universal unitary photonic devices,* Physical Review Applied **10**, 1 (2018), arXiv:1808.00458.

[16] Michael Y.-S. Fang, Sasikanth Manipatruni, Casimir Wierzynski, Amir Khosrowshahi, and Michael R. DeWeese, *Design of optical neural networks with component imprecisions,* Optics Express **27**, 14009 (2019).

[17] Ryan Hamerly, Saumil Bandyopadhyay, and Dirk Englund, *Stability of Self-Configuring Large Multiport Interferometers,* (2021), arXiv:2106.04363.

[18] S. A. Fldzhyan, M. Yu. Saygin, and S. P. Kulik, *Optimal design of error-tolerant reprogrammable multiport interferometers,* Optics Letters **45**, 2632 (2020).

[19] Ryota Tanomura, Rui Tang, Toshikazu Umezaki, Go Soma, Takuo Tanemura, and Yoshiaki Nakano, *Scalable and robust photonic integrated unitary converter based on multiplane light conversion,* Physical Review Applied **17**, 024071 (2022), arXiv:2103.14782.

[20] Sean Molesky, Zin Lin, Alexander Y Piggott, Weiliang Jin, Jelena Vucković, and Alejandro W Rodriguez, *Inverse design in nanophotonics,* Nature Photonics **12**, 659 (2018).

[21] Giulia Marcucci, Davide Pierangeli, Pepijn W. H. Pinkse, Mehul Malik, and Claudio Conti, *Programming multilevel quantum gates in disordered computing reservoirs via machine learning,* Optics Express **28**, 14018 (2020),

arXiv:1905.05264.
[22] Jean-François Morizur, Lachlan Nicholls, Pu Jian, Seiji Armstrong, Nicolas Treps, Boris Hage, Magnus Hsu, Warwick Bowen, Jiri Janousek, and Hans-A Bachor, *Programmable unitary spatial mode manipulation,* Journal of the Optical Society of America A **27**, 2524 (2010), arXiv:1005.3366.
[23] Guillaume Labroille, Bertrand Denolle, Pu Jian, Philippe Genevaux, Nicolas Treps, Jean-François François Morizur, Philippe Genevaux, and Nicolas Treps, *Efficient and mode selective spatial mode multiplexer based on multi-plane light conversion,* Optics Express **22**, 15599 (2014), arXiv:1404.6455v1.
[24] Nicolas K Fontaine, Roland Ryf, Haoshuo Chen, David T Neilson, Kwangwoong Kim, and Joel Carpenter, *Laguerre-Gaussian mode sorter,* Nature Communications **10**, 1865 (2019).
[25] T Hashimoto, T Saida, I Ogawa, M Kohtoku, T Shibata, and H Takahashi, *Optical circuit design based on a wavefront-matching method,* Optics Letters **30**, 2620 (2005).
[26] Manuel Erhard, Mehul Malik, Mario Krenn, and Anton Zeilinger, *Experimental greenberger–horne–zeilinger entanglement beyond qubits,* Nature Photonics **12**, 759–764 (2018).
[27] Mario Krenn, Mehul Malik, Robert Fickler, Radek Lapkiewicz, and Anton Zeilinger, *Automated Search for new Quantum Experiments,* Physical Review Letters **116**, 1 (2016), arXiv:1509.02749.
[28] Alexey A Melnikov, Hendrik Poulsen Nautrup, Mario Krenn, Vedran Dunjko, Markus Tiersch, Anton Zeilinger, and Hans J Briegel, *Active learning machine learns to create new quantum experiments,* Proceedings of the National Academy of Sciences **115**, 1221 (2018).
[29] Mario Krenn, Manuel Erhard, and Anton Zeilinger, *Computer-inspired quantum experiments,* Nature Reviews Physics **2**, 649 (2020), arXiv:2002.09970.
[30] Han-Sen Zhong, Hui Wang, Yu-Hao Deng, Ming-Cheng Chen, Li-Chao Peng, Yi-Han Luo, Jian Qin, Dian Wu, Xing Ding, Yi Hu, *et al.*, *Quantum computational advantage using photons,* Science **370**, 1460 (2020).
[31] Daniel Llewellyn, Yunhong Ding, Imad I Faruque, Stefano Paesani, Davide Bacco, Raffaele Santagati, Yan-Jun Qian, Yan Li, Yun-Feng Xiao, Marcus Huber, and et al., *Chip-to-chip quantum teleportation and multi-photon entanglement in silicon,* Nature Physics **16**, 148–153 (2020).
[32] Xiao-Min Hu, Yu Guo, Bi-Heng Liu, Yun-Feng Huang, Chuan-Feng Li, and Guang-Can Guo, *Beating the channel capacity limit for superdense coding with entangled ququarts,* Science Advances **4**, eaat9304 (2018).
[33] Sebastian Ecker, Frédéric Bouchard, Lukas Bulla, Florian Brandt, Oskar Kohout, Fabian Steinlechner, Robert Fickler, Mehul Malik, Yelena Guryanova, Rupert Ursin, and Marcus Huber, *Overcoming Noise in Entanglement Distribution,* Physical Review X **9**, 041042 (2019), arXiv:1904.01552.
[34] Feng Zhu, Max Tyler, Natalia Herrera Valencia, Mehul Malik, and Jonathan Leach, *Is high-dimensional photonic entanglement robust to noise?* AVS Quantum Science **3**, 011401 (2021), arXiv:1908.08943.
[35] Tamás Vertesi, Stefano Pironio, and Nicolas Brunner, *Closing the Detection Loophole in Bell Experiments Using Qudits,* Phys. Rev. Lett. **104**, 60401 (2010), arXiv:0909.3171.
[36] Vatshal Srivastav, Natalia Herrera Valencia, Will McCutcheon, Saroch Leedumrongwatthanakun, Sébastien Designolle, Roope Uola, Nicolas Brunner, and Mehul Malik, *Noise-robust and loss-tolerant quantum steering with qudits,* (2022), arXiv:2202:09294.
[37] Natalia Herrera Valencia, Suraj Goel, Will McCutcheon, Hugo Defienne, and Mehul Malik, *Unscrambling entanglement through a complex medium,* Nature Physics **16**, 1112 (2020), arXiv:1910.04490.
[38] Huan Cao, She-Cheng Gao, Chao Zhang, Jian Wang, De-Yong He, Bi-Heng Liu, Zheng-Wei Zhou, Yu-Jie Chen, Zhao-Hui Li, Si-Yuan Yu, and et al., *Distribution of high-dimensional orbital angular momentum entanglement over a 1 km few-mode fiber,* Optica **7**, 232–237 (2020).
[39] Jessica Bavaresco, Natalia Herrera Valencia, Claude Klöckl, Matej Pivoluska, Paul Erker, Nicolai Friis, Mehul Malik, and Marcus Huber, *Measurements in two bases are sufficient for certifying high-dimensional entanglement,* Nat. Phys. **14**, 1032 (2018), arXiv:1709.07344.
[40] Nicolai Friis, Giuseppe Vitagliano, Mehul Malik, and Marcus Huber, *Entanglement certification from theory to experiment,* Nature Reviews Physics **1**, 72 (2019).
[41] Natalia Herrera Valencia, Vatshal Srivastav, Matej Pivoluska, Marcus Huber, Nicolai Friis, Will McCutcheon, and Mehul Malik, *High-Dimensional Pixel Entanglement: Efficient Generation and Certification,* Quantum **4**, 376 (2020), arXiv:2004.04994.
[42] Amin Babazadeh, Manuel Erhard, Feiran Wang, Mehul Malik, Rahman Nouroozi, Mario Krenn, and Anton Zeilinger, *High-Dimensional Single-Photon Quantum Gates: Concepts and Experiments,* Physical Review Letters **119**, 180510 (2017), arXiv:1702.07299.
[43] Feiran Wang, Manuel Erhard, Amin Babazadeh, Mehul Malik, Mario Krenn, and Anton Zeilinger, *Generation of the complete four-dimensional Bell basis,* Optica **4**, 1462 (2017), arXiv:1707.05760.
[44] Florian Brandt, Markus Hiekkamäki, Frédéric Bouchard, Marcus Huber, and Robert Fickler, *High-dimensional quantum gates using full-field spatial modes of photons,* Optica , 98 (2020), arXiv:1907.13002.
[45] Ohad Lib, Kfir Sulimany, and Yaron Bromberg, *Reconfigurable synthesizer for quantum information processing of high-dimensional entangled photons,* (2021), arXiv:2108.02258.
[46] Stefan Rotter and Sylvain Gigan, *Light fields in complex media: Mesoscopic scattering meets wave control,* Reviews of Modern Physics **89**, 015005 (2017), arXiv:1702.05395.
[47] Hui Cao and Yaniv Eliezer, *Harnessing disorder for photonic device applications,* Applied Physics Reviews **9**, 011309 (2022).
[48] Simon R. Huisman, Thomas J. Huisman, Tom A. W. Wolterink, Allard P. Mosk, and Pepijn W. H. Pinkse, *Programmable multiport optical circuits in opaque scattering materials,* Optics Express **23**, 3102 (2015), arXiv:1408.1856.
[49] Maxime W. Matthès, Philipp del Hougne, Julien de Rosny, Geoffroy Lerosey, and Sébastien M. Popoff, *Optical complex media as universal reconfigurable linear operators,* Optica **6**, 465 (2019).
[50] Tom A. W. Wolterink, Ravitej Uppu, Georgios Ctistis, Willem L. Vos, Klaus J. Boller, and Pepijn W. H. Pinkse, *Programmable two-photon quantum interference in* 10^3

channels in opaque scattering media, Physical Review A **93**, 053817 (2015), arXiv:1511.00897.

[51] Hugo Defienne, Marco Barbieri, Ian A. Walmsley, Brian J. Smith, and Sylvain Gigan, *Two-photon quantum walk in a multimode fiber,* Science Advances **2**, e1501054 (2016), arXiv:1504.03178.

[52] Saroch Leedumrongwatthanakun, Luca Innocenti, Hugo Defienne, Thomas Juffmann, Alessandro Ferraro, Mauro Paternostro, and Sylvain Gigan, *Programmable linear quantum networks with a multimode fibre,* Nature Photonics **14**, 139 (2020), arXiv:1902.10678.

[53] Natalia Herrera Valencia, Vatshal Srivastav, Saroch Leedumrongwatthanakun, Will McCutcheon, and Mehul Malik, *Entangled ripples and twists of light: radial and azimuthal laguerre–gaussian mode entanglement,* Journal of Optics **23**, 104001 (2021).

[54] Frédéric Bouchard, Natalia Herrera Valencia, Florian Brandt, Robert Fickler, Marcus Huber, and Mehul Malik, *Measuring azimuthal and radial modes of photons,* Opt. Express **26**, 31925 (2018), arXiv:1808.03533.

[55] Jason P Allmaras, Emma E Wollman, Andrew D Beyer, Ryan M Briggs, Boris A Korzh, Bruce Bumble, and Matthew D Shaw, *Demonstration of a thermally coupled row-column snspd imaging array,* Nano Letters **20**, 2163–2168 (2020).

[56] Sébastien Designolle, Vatshal Srivastav, Roope Uola, Natalia Herrera Valencia, Will McCutcheon, Mehul Malik, and Nicolas Brunner, *Genuine high-dimensional quantum steering,* Physical Review Letters **126**, 200404 (2021).

[57] David A. B. Miller, *All linear optical devices are mode converters,* Optics Express **20**, 23985 (2012), arXiv:1209.4931.

[58] David A. B. Miller, *Waves, modes, communications, and optics: a tutorial,* Advances in Optics and Photonics **11**, 679 (2019).

[59] Joel Carpenter, Benjamin J. Eggleton, and Jochen Schröder, *110X110 Optical Mode Transfer Matrix Inversion,* Optics Express **22**, 96 (2014).

[60] Martin Plöschner, Tomáš Tyc, and Tomáš Čižmár, *Seeing through chaos in multimode fibres,* Nature Photonics **9**, 529 (2015).

[61] Wen Xiong, Chia Wei Hsu, Yaron Bromberg, Jose Enrique Antonio-Lopez, Rodrigo Amezcua Correa, and Hui Cao, *Complete polarization control in multimode fibers with polarization and mode coupling,* Light: Science & Applications **7**, 54 (2018), arXiv:1709.01029.

[62] Y. Sakamaki, T. Saida, T. Hashimoto, and H. Takahashi, *New Optical Waveguide Design Based on Wavefront Matching Method,* Journal of Lightwave Technology **25**, 3511 (2007).

[63] Nicolas K. Fontaine, Roland Ryf, Haoshuo Chen, David Neilson, and Joel Carpenter, *Design of High Order Mode-Multiplexers using Multiplane Light Conversion,* in *2017 European Conference on Optical Communication (ECOC)*, Vol. 2017-Septe (IEEE, 2017) pp. 1–3.

[64] J B Altepeter, D Branning, E Jeffrey, T C Wei, P G Kwiat, R T Thew, J L O'Brien, M A Nielsen, and A. G. White, *Ancilla-assisted quantum process tomography,* Physical Review Letters **90**, 193601 (2003).

[65] Hammam Qassim, Filippo M Miatto, Juan P Torres, Miles J Padgett, Ebrahim Karimi, and Robert W Boyd, *Limitations to the determination of a Laguerre-Gauss spectrum via projective, phase-flattening measurement,* J. Opt. Soc. Am. B **31**, A20 (2014), arXiv:1401.3512.

[66] M. Yu. Saygin, I. V. Kondratyev, I. V. Dyakonov, S. A. Mironov, S. S. Straupe, and S. P. Kulik, *Robust Architecture for Programmable Universal Unitaries,* Physical Review Letters **124**, 010501 (2020), arXiv:1906.06748.

[67] Luciano Pereira, Alejandro Rojas, Gustavo Cañas, Gustavo Lima, Aldo Delgado, and Adán Cabello, *Universal multi-port interferometers with minimal optical depth,* (2020), arXiv:2002.01371.

[68] Roman Bruck, Kevin Vynck, Philippe Lalanne, Ben Mills, David J. Thomson, Goran Z. Mashanovich, Graham T. Reed, and Otto L. Muskens, *All-optical spatial light modulator for reconfigurable silicon photonic circuits,* Optica **3**, 396 (2016), arXiv:1601.06679.

[69] Zi Wang, Tiantian Li, Anishkumar Soman, Dun Mao, Thomas Kananen, and Tingyi Gu, *On-chip wavefront shaping with dielectric metasurface,* Nature Communications **10**, 3547 (2019).

[70] Nicholas J. Dinsdale, Peter R. Wiecha, Matthew Delaney, Jamie Reynolds, Martin Ebert, Ioannis Zeimpekis, David J. Thomson, Graham T. Reed, Philippe Lalanne, Kevin Vynck, and Otto L. Muskens, *Deep Learning Enabled Design of Complex Transmission Matrices for Universal Optical Components,* ACS Photonics **8**, 283 (2021), arXiv:2009.11810.

[71] Joseph M. Lukens, Pavel Lougovski, J Oseph M L Ukens, P Avel L Ougovski, Joseph M. Lukens, and Pavel Lougovski, *Frequency-encoded photonic qubits for scalable quantum information processing,* Optica **4**, 2 (2016), arXiv:1612.03131.

[72] Mickael Mounaix, Daria Andreoli, Hugo Defienne, Giorgio Volpe, Ori Katz, Samuel Grésillon, and Sylvain Gigan, *Spatiotemporal coherent control of light through a multiple scattering medium with the multispectral transmission matrix,* Physical review letters **116**, 253901 (2016).

[73] Hsuan-hao Lu, Joseph M Lukens, Nicholas A Peters, Ogaga D. Odele, Daniel E Leaird, Andrew M Weiner, and Pavel Lougovski, *Electro-Optic Frequency Beam Splitters and Tritters for High-Fidelity Photonic Quantum Information Processing,* Physical Review Letters **120**, 30502 (2018).

[74] Mickael Mounaix, Nicolas K. Fontaine, David T. Neilson, Roland Ryf, Haoshuo Chen, Juan Carlos Alvarado-Zacarias, and Joel Carpenter, *Time reversed optical waves by arbitrary vector spatiotemporal field generation,* Nature Communications **11**, 5813 (2020).

[75] Fabio Crameri, *Scientific colour maps,* (2021).

[76] Vatshal Srivastav, Natalia Herrera Valencia, Saroch Leedumrongwatthanakun, Will McCutcheon, and Mehul Malik, *Characterising and Tailoring Spatial Correlations in Multi-Mode Parametric Downconversion,* (2021), arXiv:2110.03462.

[77] Jessica Bavaresco, Natalia Herrera Valencia, Claude Klockl, Matej Pivoluska, Paul Erker, Nicolai Friis, Mehul Malik, and Marcus Huber, *Measurements in two bases are sufficient for certifying high-dimensional entanglement,* Nature Physics **14**, 1032 (2018).

[78] Natalia Herrera Valencia, Vatshal Srivastav, Saroch Leedumrongwatthanakun, Will McCutcheon, and Mehul Malik, *Entangled ripples and twists of light: radial and azimuthal Laguerre–Gaussian mode entanglement,* Journal of Optics **23**, 104001 (2021), arXiv:2104.04506.

[79] Piergiorgio Caramazza, Oisín Moran, Roderick Murray-Smith, and Daniele Faccio, *Transmission of natural*

scene images through a multimode fibre, Nature communications **10**, 1 (2019).

[80] Victor Arrizon, Ulises Ruiz, Rosibel Carrada, and Luis A Gonzalez, *Pixelated phase computer holograms for the accurate encoding of scalar complex fields,* J. Opt. Soc. Am. A **24**, 3500 (2007).

[81] W.K. Wootters and B.D. Fields, *Optimal state-determination by mutually unbiased measurements,* Ann. Phys. (N. Y). **191**, 363 (1989).

[82] D. Giovannini, J. Romero, J. Leach, A. Dudley, A. Forbes, and M. J. Padgett, *Characterization of high-dimensional entangled systems via mutually unbiased measurements,* Physical Review Letters **110** (2013), arXiv:1212.5825.

[83] Suraj Goel, Saroch Leedumrongwatthanakun, Natalia Herrera Valencia, Will McCutcheon, Claudio Conti, Pepijn W. H. Pinkse, and Mehul Malik, *Simulation codes for : Inverse-design of high-dimensional quantum optical circuits in a complex medium,* (2022).

[84] Unter, Z. I. Borevich, and S. L. Krupetskii, *Subgroups of the unitary group that contain the group of diagonal matrices,* Journal of Soviet Mathematics **17**, 1951 (1981).

[85] Pauline Boucher, Arthur Goetschy, Giacomo Sorelli, Mattia Walschaers, and Nicolas Treps, *Full characterization of the transmission properties of a multi-plane light converter,* Physical Review Research **3**, 1 (2020), arXiv:2005.11982.

[86] Michael Schmid, Rainer Steinwandt, Jörn Müller-Quade, Martin Rötteler, and Thomas Beth, *Decomposing a matrix into circulant and diagonal factors,* Linear Algebra and Its Applications **306**, 131 (2000).

[87] Marko Huhtanen and Allan Perämäki, *Factoring Matrices into the Product of Circulant and Diagonal Matrices,* Journal of Fourier Analysis and Applications **21**, 1018 (2015).

[88] Martin Idel and Michael M. Wolf, *Sinkhorn normal form for unitary matrices,* Linear Algebra and Its Applications **471**, 76 (2015), arXiv:1408.5728.

[89] Víctor López Pastor, Jeff Lundeen, and Florian Marquardt, *Arbitrary optical wave evolution with Fourier transforms and phase masks,* Optics Express **29**, 38441 (2021), arXiv:1912.04721.

Supplementary information for: Inverse-design of high-dimensional quantum optical circuits in a complex medium

The following supplementary information is provided: Details of the high-dimensionally entangled two-photon source (S.1), acquisition of transfer matrix (S.2), projective measurements and detection efficiency (S.3), quantum state tomography (S.4), construction of linear circuits (S.5), and analysis of fidelity, success probability and optical losses (S.6). The supplementary results on manipulation of the high-dimensional entangled states using various types of gates in the macro-pixel and the orbital-angular-momentum (OAM) bases are presented in (S.7). Finally, numerical results on the programmability and scalability of our gates are reported in (S.8).

S.1. High-dimensional two-photon entanglement source

The high-dimensional spatially entangled two-photon state is generated via degenerate Type-II spontaneous parametric downconversion (SPDC) by pumping a 15-mm long periodically poled Potassium Titanyl Phosphate (ppKTP) crystal with a 405nm continuous-wave laser. After passing through the long-pass dichroic filter and the band-pass filter, the signal and idler photons are separated using a polarising-beam-splitter (PBS) and are mapped on to the liquid-crystal-on-silicon-based spatial light modulators (SLM) (P_1 and P_3) which are placed in the Fourier plane of the ppKTP crystal. The main characteristics of the entanglement source, i.e., the strength of transverse-momentum correlation, generated beam waist, and the position of the beams, are determined by using our developed $2D\pi$-measurement [76] which is the joint coincidence measurement of local π-phase step knife-edge scans across the SLMs at each party. The two-photon state is then characterised via quantum state tomography (S.4) and the entanglement dimensionality is certified [77] using a high-dimensional entanglement witness in two discrete spatial-mode bases—the Macro-pixel basis [41] and the orbital-angular-momentum (OAM) basis [78]. We utilise these two bases as the set of input target modes for constructing the programmable circuits. For the macro-pixel basis, the size of pixels and their spacing are determined by the joint transverse momentum amplitude (JTMA) [76]. For the OAM basis, the set of modes are $\{|-\ell\rangle,\ldots,|0\rangle,\ldots,|\ell\rangle\}$ when the dimension of the circuit d is odd, otherwise $\{|-\ell\rangle,\ldots,|-1\rangle,|1\rangle,\ldots,|\ell\rangle\}$. The measured quantifiers of the generated high-dimensionally entangled two-photon states are reported in Table S.1 and the reconstructed density matrices are depicted in Fig. S.1 and Fig. S.2 for the macro-pixel and OAM bases, respectively.

Table S.1: Generated high-dimensionally entangled two-photon states: State purity $\mathcal{P}$, Entanglement dimensionality d_{ent}, Fidelity to maximally entangled state $\mathcal{F}$, Entanglement of Formation (E_{oF}). Errors are calculated as 3 standard deviations assuming Poisson statistics in photon counts.

Basis	Dimension (d)	$\mathcal{P}$	d_{ent}	$\mathcal{F}(\rho_i, \lvert\Phi^+\rangle\langle\Phi^+\rvert)$	E_{oF} (ebits)
Macro-Pixel	2	96.7 ± 0.7 %	2	96.8 ± 0.4 %	0.80 ± 0.02
	3	92.6 ± 0.4 %	3	95.3 ± 0.2 %	1.23 ± 0.01
	5	88.8 ± 0.3 %	5	91.6 ± 0.2 %	1.51 ± 0.02
	7	75.1 ± 0.3 %	6	83.0 ± 0.2 %	1.19 ± 0.01
OAM	2	97.7 ± 0.2 %	2	97.5 ± 0.1 %	0.81 ± 0.01
	3	85.9 ± 0.2 %	3	90.8 ± 0.1 %	1.11 ± 0.01
	5	83.2 ± 0.2 %	5	86.5 ± 0.1 %	1.19 ± 0.01
	7	80.0 ± 0.1 %	6	80.6 ± 0.1 %	1.11 ± 0.01

S.2. Acquisition of transfer matrix

To construct the circuits, the optical apparatus is described by the transfer matrix: $\mathbf{T} = U_2 P_2 U_1 P_1$, where U_2 is a $2f$ lens system and P_j is the j-th phase plane displayed on the SLM$_j$. The transfer matrix U_1 of the 2m-long graded-index multi-mode fiber (Thorlabs-M116L02) and associated coupling optics between the first and second phase planes (P_1 and P_2) in a single linear-polarisation channel is measured without using an external reference field. To do so, we search for the transfer matrix U_1 by optimising

$$\min \left| I_i - |U_2 P_2 U_1 P_1|^2 \right|^2 . \tag{S.2.1}$$

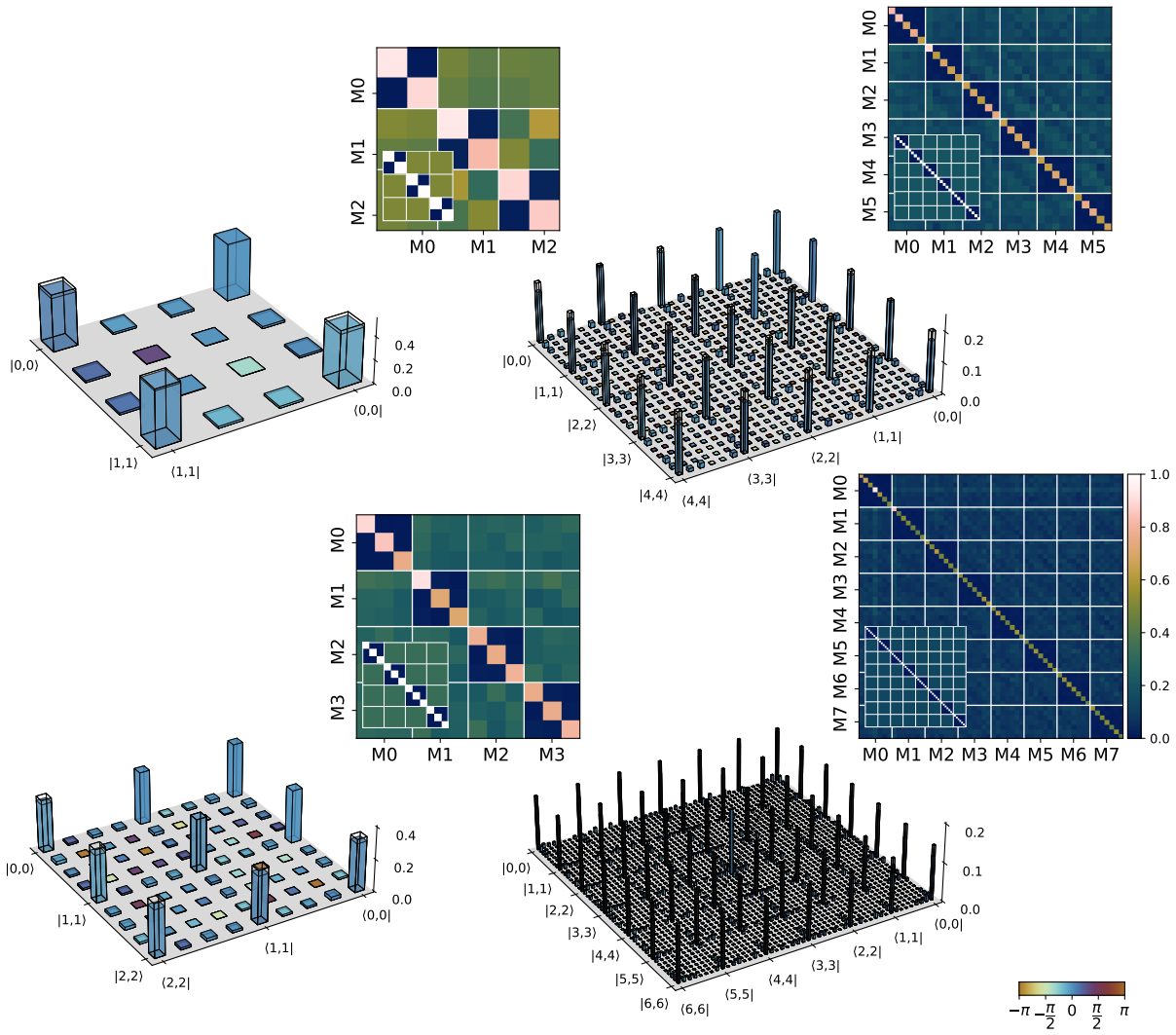

Figure S.1. **Generated high-dimensional entangled two-photon states in the macro-pixel basis.** Measured coincidence counts in all mutually unbiased bases (MUBs) and reconstructed density matrices via quantum state tomography in dimensions, $d = [2, 3, 5, 7]$.

The optimisation is based on the gradient descent method fitting the acquired characterisation data consisting of random phase patterns displayed on SLM_1 and SLM_2 and the corresponding measured output speckle intensity images $\{I_i\}_i$. The model of the optical apparatus is implemented in Keras using Tensorflow2 and complex-number layers developed in [79]. The data set is prepared in three parts. In the first part, each input mode in a given basis that is supported by the fiber is displayed on SLM_1. This data provides accurate information of $|U_1|$. In the second part, random superpositions of these input modes are prepared on SLM_1 and sent through the fibre. The output intensity speckles in this part allow for recovery of the relative phase and amplitude of transmission coefficient for a particular output mode. Finally, both SLMs are used for displaying random superpositions of the input modes and output modes. This final part of the data set allows for accurate reconstruction of U_1, including calibration of the unknown relative phases across the output modes.

S.3. Projective measurements and detection efficiency

The characterisation of the entangled light source both before and after manipulation by the circuits is performed by local projective measurements. The computer-generated hologram (CGH) [80] for a particular spatial mode is

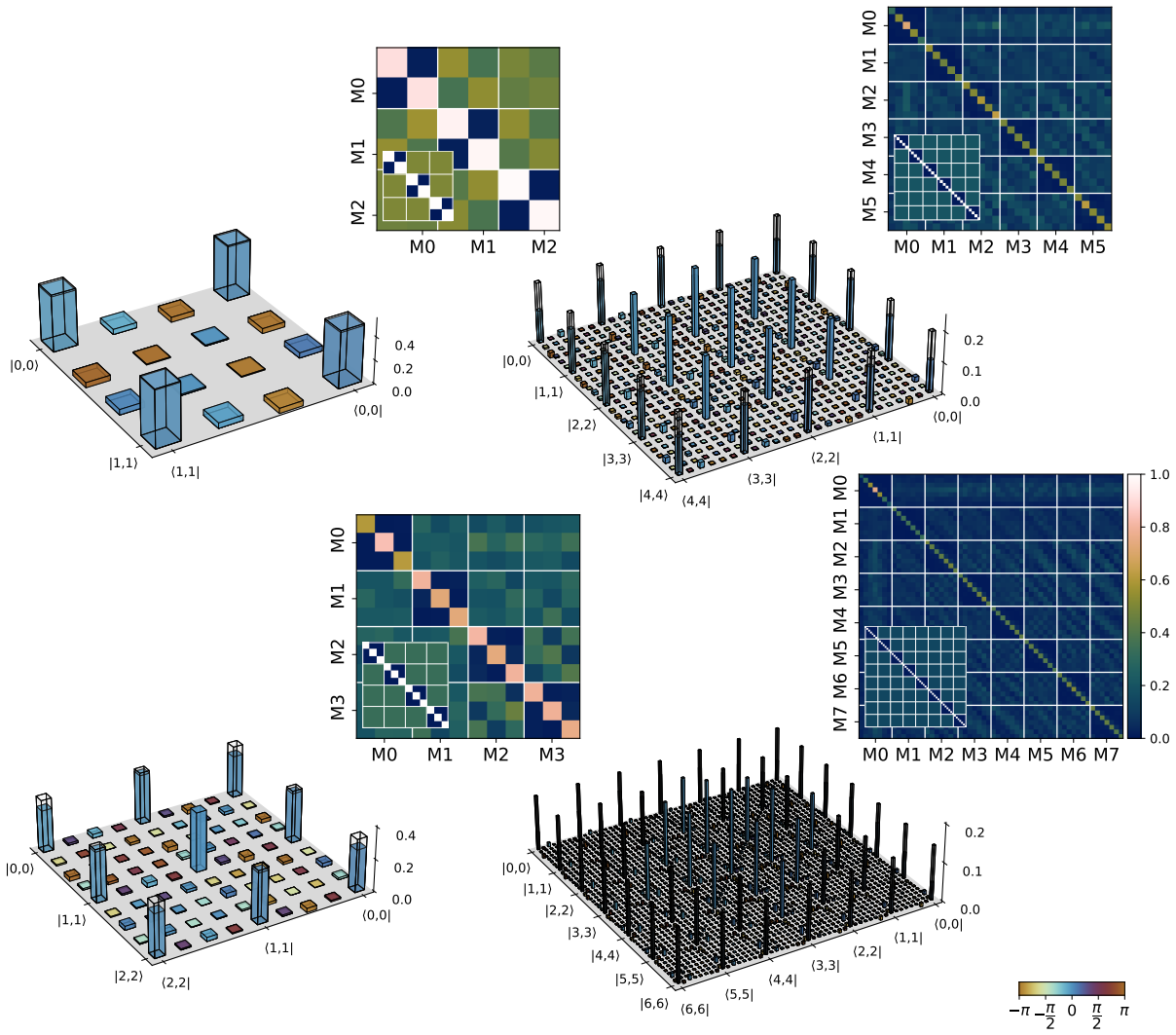

Figure S.2. **Generated high-dimensionally entangled two-photon states in the OAM basis.** Measured coincidence counts in all mutually unbiased bases (MUBs) and reconstructed density matrices via quantum state tomography in dimensions, $d = [2, 3, 5, 7]$.

displayed on the SLM at each party. If the incident spatial mode is the complex conjugate of the hologram mode, it is converted into a Gaussian mode, which couples efficiently into a single-mode fiber (SMF) positioned in the 1st-order diffraction spot. Coincidence events between the detection of signal and idler photons in the selected modes is registered by the coincidence logic within a coincidence window of 0.2 ns. The detection efficiency η_a^μ of measuring a particular spatial mode, $|\psi_a^\mu\rangle$ (corresponding to the a-th element of the μ-th basis), is estimated and the performed measurements are then related to ideal projections by $\hat{\tilde{\Pi}}_a^\mu = \eta_a^\mu \hat{\Pi}_a^\mu$, where $\hat{\Pi}_a^\mu = |\psi_a^\mu\rangle\langle\psi_a^\mu|$ is the ideal projector.

S.4. Quantum state tomography

Quantum state tomography (QST) is performed through the measurement of an informationally complete set of measurements and numeric inversion of the data, subject to physical constraints. It provides full characteristic information about a state, and via performing QST on both the input and output states we can characterise the implemented optical circuit. We perform QST via semidefinite programming (SDP) on both input and output states after manipulation by the optical circuits. The SDP imposes data fitting of the non-normalised measurements subject

to positive semi-definitness of the state ρ, and unit trace, and reads as

$$\begin{aligned} \min_{\rho,R} \quad & |\mathcal{C}_{ab}^{\mu\nu} - R\mathrm{Tr}(\hat{\tilde{\Pi}}_a^{\mu} \otimes \hat{\tilde{\Pi}}_b^{\nu} \rho)|^2 \\ \text{s.t.} \quad & \rho \geq 0\,,\ \mathrm{Tr}[\rho] = 1, \end{aligned} \tag{S.4.1}$$

where $\mathcal{C}_{ab}^{\mu\nu}$ is the frequency of the outcome (coincidence count rate) and R is the count rate per integration window. Our local measurement bases are complete sets of mutually unbiased bases (MUBs) [81], which are informationally complete for QST [82], and constructed as : $\hat{\Pi}_a^{\mu} = |M_a^{\mu}\rangle\langle M_a^{\mu}|$ and $\hat{\Pi}_b^{\nu} = |M_b^{\nu *}\rangle\langle M_b^{\nu *}|$, where $|M_a^{\mu}\rangle = \frac{1}{\sqrt{d}} \sum_{m=0}^{d-1} \omega_d^{am+\mu m^2} |m\rangle$ on the basis of each implemented circuit, and $\omega_d = \exp(2\pi i/d)$ is a d-th root of unity. All SDPs are implemented in CVX, running the commercial solver MOSEK.

S.5. Construction of linear circuits

Primarily, programming a circuit $\mathbb{T}$ is achieved by calculating the phase solutions $\{P_j\}_{j=1}^{L}$ at each phase plane. The wavefront matching algorithm (WFM) can do so by iteratively matching the wavefronts of target input and output optical modes propagating through the device across all phase planes [25, 62, 63]. First, input arguments that contain a set of input spatial modes $\{|\psi_a(\mathbf{q})\rangle\}_{a=0}^{d-1}$ labelled in the logical basis by $\{|a\rangle_{\text{in}}\}_{a=0}^{d-1}$, a corresponding set of output spatial modes $\{|\phi_a(\mathbf{q})\rangle\}_{a=0}^{d-1}$ that is related to the inputs via $|a_{\text{out}}\rangle = \mathbb{T}|a_{\text{in}}\rangle$, and a set of transfer functions $\{U_j\}$ between phase planes are provided to the WFM algorithm.

For each i-th iteration, a phase solution at the p-th plane is updated in a cyclic manner starting from the first to the last L-th plane and then back from the last plane to the first. At a particular reconfigurable phase plane P_p, the transfer matrix of the optical device $\mathbf{T}$ represented in the spatial $\mathbf{q}$ basis is decomposed into two sections:

$$\mathbf{T} := \prod_{j=1}^{L} U_j P_j = B_p P_p F_p, \tag{S.5.1}$$

where $B_p = \prod_{j=p}^{L} P_{j+1} U_j$ and $F_p = \prod_{j=1}^{p-1} U_j P_j$ such that the forward-propagating input mode onto the p-th phase plane is represented by $|\psi_{a,(p)}\rangle = F_p|\psi_a\rangle$ and the backward-propagating output mode onto the p-th phase plane is $|\phi_{a,(p)}\rangle = B_p^{\dagger}|\phi_a\rangle$. The phase mismatch between these input and output modes can then be adjusted by P_p:

$$|\phi_a\rangle = B_p P_p F_p |\psi_a\rangle \implies |\phi_{a,(p)}\rangle = P_p |\psi_{a,(p)}\rangle\,. \tag{S.5.2}$$

Considering all d-target modes of interest, the *matching* matrix: $M_p := \sum_{a,a'=0}^{d-1} \langle\phi_{a',(p)}|P_p|\psi_{a,(p)}\rangle |a'\rangle\langle a|$ captures the mode mixing at each phase plane. The WFM algorithm maximise $\mathrm{Tr}(M_p)$ by calculating a phase solution $P_p^{[i]}$ from the weighed average of overlapped fields over all d-target modes as follows:

$$P_p^{[i]}(\mathbf{q}) = \exp\left(i \arg\left(\sum_{a=0}^{d-1} \phi_{a,(p)}^{[\text{latest}]}(\mathbf{q}) \odot \psi_{a,(p)}^{*[\text{latest}]}(\mathbf{q})\right)\right), \tag{S.5.3}$$

where $\odot$ is an element-wise multiplication on the $\mathbf{q}$ coordinate (SLM pixels) and $\phi_{a,(p)}^{[\text{latest}]}(\mathbf{q})$ and $\psi_{a,(p)}^{*[\text{latest}]}(\mathbf{q})$ is the latest update of output and input optical fields at the p-th phase plane taking into account all other previous updated phase planes $\{P_p^{[i]}\}$ in the current iteration in both forward and backward directions. The algorithm is iterated until an appropriate value of gate fidelity (Eq. S.6.2) is achieved or saturated.

In our experiment, the following gates $\mathbb{T}$ are implemented and defined as:

$$\mathbb{I} = \sum_{a=0}^{d-1} |a\rangle\langle a|, \qquad \mathbb{Z} = \sum_{a=0}^{d-1} |a\rangle\omega_d^a\langle a|, \qquad \mathbb{X} = \sum_{a=0}^{d-1} |a\oplus 1\rangle\langle a|, \qquad \mathbb{F} = \frac{1}{\sqrt{d}} \sum_{a,b=0}^{d-1} |b\rangle\omega_d^{ab}\langle a|, \tag{S.5.4}$$

where $\omega_d = \exp(2\pi i/d)$ and $a \oplus 1 := (a+1) \mod d$. $\mathbb{R}$ is the random unitary which is sampled from the Haar measure for each implementation.

S.6. Fidelity, success probability and optical losses

We use two figures of merit to characterise the implemented circuits—fidelity $\mathcal{F}$ and success probability $\mathcal{S}$. The first is the Uhlmann-Josza fidelity between two density matrices:

$$\mathcal{F}(\rho,\rho_{\mathrm{o}}) \coloneqq \left(\mathrm{Tr}\left(\sqrt{\sqrt{\rho}\rho_{\mathrm{o}}\sqrt{\rho}}\right)\right)^2, \tag{S.6.1}$$

where ρ_{o} is the experimental density matrix of the manipulated state supported on the space of the circuit and ρ is the output density matrix of initial state ρ_{i} manipulated by theoretical ideal target circuit $\mathbb{T}$: $\rho = (\mathbb{I}\otimes\mathbb{T})\rho_{\mathrm{i}}(\mathbb{I}\otimes\mathbb{T}^\dagger)$. The fidelity thus implies an accuracy of the implemented circuits. Noting that, in the case that the initial maximally entangled state is pure ($\mathcal{P} \coloneqq \mathrm{Tr}\left(\rho_{\mathrm{i}}^2\right) = 1$) and the implemented circuit can be represented by a rank-one Kraus operator $\widetilde{\mathbb{T}}$, the fidelity reduces to:

$$\mathcal{F} = \frac{\left(\mathrm{Tr}\left(\widetilde{\mathbb{T}}^\dagger\mathbb{T}\right)\right)^2}{\mathrm{Tr}\left(\widetilde{\mathbb{T}}^\dagger\widetilde{\mathbb{T}}\right)\mathrm{Tr}\left(\mathbb{T}^\dagger\mathbb{T}\right)}, \tag{S.6.2}$$

which is normalised by the transmittance due to the scattering from the d-dimensional space of a circuit into other optical modes. The transmittance is quantified by the second figure of merit, the success probability, $\mathcal{S}$, of an implemented circuit:

$$\mathcal{S} \coloneqq \frac{\mathrm{Tr}\left(\widetilde{\mathbb{T}}^\dagger\widetilde{\mathbb{T}}\right)}{\mathrm{Tr}\left(\mathbb{T}^\dagger\mathbb{T}\right)}, \tag{S.6.3}$$

The implemented d-dimensional circuit $\widetilde{\mathbb{T}}$ is embedded in $\mathbf{T}$ which lives in the n-dimensional space of the apparatus such that: $\widetilde{\mathbb{T}} = \mathbf{P}_{\mathrm{o}}\mathbf{T}\mathbf{P}_{\mathrm{i}}$, where $\mathbf{P}_{\mathrm{o}}$ is the output dimensional reduction and $\mathbf{P}_{\mathrm{i}}$ is the input dimensional expansion, which map the circuit from d inputs of interest to n inputs of the optical device and from n outputs of the optical device to the d output modes of circuit, respectively. We aim to use $\mathcal{S}$ to measure the scattering loss which stems from the effect of the top-down circuit design, whereas another optical loss of the apparatus is analysed in the last part of this section. Experimentally, the success probability $\mathcal{S}$ (Eq. S.6.3) is estimated on the output $\mathbf{x}$ space as

$$\mathcal{S} = \frac{1}{d}\sum_{a=0}^{d-1}\int d^2\mathbf{x}\left|\sum_{b=0}^{d-1}\widetilde{t}_{ab}\phi_b(\mathbf{x})\right|^2 = \frac{1}{d}\sum_{a=0}^{d-1}\int d^2\mathbf{x}\sum_{b=0}^{d-1}\frac{\mathcal{I}_{ab}}{\mathcal{I}_a}\left|\phi_b(\mathbf{x})\right|^2, \tag{S.6.4}$$

where $\widetilde{t}_{ab}$ is a transmission coefficient given that $\widetilde{\mathbb{T}} = \sum_{a,b=0}^{d-1}\widetilde{t}_{ab}\left|b\right\rangle\left\langle a\right|$ and $\phi_b(\mathbf{x})$ is the b-th standard output optical field of circuit on the output $\mathbf{x}$ space. The normalisation of $\widetilde{t}_{ab}$ is measured by the ratio of optical flux inside the b-th output mode of a circuit, $\mathcal{I}_{ab} \propto |\widetilde{t}_{ab}|^2$, to total output optical flux transmitting through the system given the a-th input mode, $\mathcal{I}_a \coloneqq \int d^2\mathbf{x}\mathcal{I}_a(\mathbf{x})$ where $\mathcal{I}_a(\mathbf{x}) \propto |\sum_{b=0}^{n-1}\widetilde{t}_{ab}\phi_b(\mathbf{x})|^2$. Noting that the optical flux $\mathcal{I}_{ab}$ can be moved outside the bracket because the target outputs are foci which are spatially separated and conveniently detected using a coherent light source. For a two-photon entangled state, the success probability is then calculated in a similar way yet using the outcomes of joint measurements between Alice and Bob who has a circuit and performs the measurements via $\widehat{\widetilde{\Pi}}(\mathbf{x}) \coloneqq \eta(\mathbf{x})\left|\mathbf{x}\right\rangle\left\langle\mathbf{x}\right|$ across the output spatial $\mathbf{x}$ space:

$$\mathcal{S}^\mu = \frac{1}{d}\sum_{a=0}^{d-1}\int d^2\mathbf{x}\sum_{b=0}^{d-1}\frac{\mathcal{C}_{ab}^{\mu,\nu=0}}{\mathcal{C}_a^\mu(\mathbf{x})}\left|\phi_b(\mathbf{x})\right|^2, \tag{S.6.5}$$

where the coincidence counts ($\mathcal{C}_{ab}^{\mu,\nu=0}$ and $\mathcal{C}_a^\mu(\mathbf{x})$) are calibrated by the detection efficiencies for both parties as described in S.3. And, $\mathcal{C}_a^\mu(\mathbf{x})$ is defined as

$$\mathcal{C}_a^\mu(\mathbf{x}) = R\frac{1}{\eta_a^\mu\eta(\mathbf{x})}\mathrm{Tr}(\hat{\widetilde{\Pi}}_a^\mu\otimes\hat{\widetilde{\Pi}}(\mathbf{x})\rho_{\mathrm{o}}). \tag{S.6.6}$$

Noting that we perform the experiment on all input bases and the success probability is thus averaged over all input bases, $\mathcal{S} = \sum_{\mu=0}^{d}\mathcal{S}^\mu/(d+1)$. Moreover, one can show that Eq. S.6.5 can be reformulated back as Eq. S.6.3 in the case that the input maximally entangled state and process (circuit) are pure.

Finally, the overall transmittance $\mathcal{T}$ of a circuit is measured using the two-photon entangled state at the input and output of a circuit,

$$\mathcal{T}_a^\mu = \sum_{b=0}^{d-1}\frac{\mathcal{C}_{ab}^{\mu,\nu=0}}{\mathcal{C}^{*\mu,\nu=0}_{ab}}, \tag{S.6.7}$$

where $\mathcal{C}^{*\mu,\nu=0}_{ab}$ is the coincidence counts at the initial state. The overall transmittance, $\mathcal{T} = \mathcal{S} \times \mathcal{T}_o$, includes the success probability, $\mathcal{S}$, of a circuit and other optical transmittance of the apparatus, $\mathcal{T}_o$.

In experiment, the measurements of success probability and overall transmittance are performed in the macro-pixel input basis. The results are shown in Fig. S.3 where the averaged optical transmittance is 0.051 ± 0.008, 0.04 ± 0.006, 0.026 ± 0.004 and 0.028 ± 0.003 for 2, 3, 5 and 7-dimensional gates respectively. We performed the measurement of the success probability for 3 randomly chosen implementations of Fourier-$\mathbb{F}$ gates in $2, 3$ and 5 dimensions and observe $\mathcal{S}$ of 0.36 ± 0.014, 0.27 ± 0.03 and 0.18 ± 0.04, respectively. We thus infer an average optical transmittance of $\mathcal{T}_o = 0.14 \pm 0.02$ which is attributed to the optical insertion and propagation losses, diffraction efficiency of the two SLMs, and other interface losses at the lenses and mirrors. We note that the main contribution to the loss is due to the success probability arising from control of only a single polarisation channel of the multi-mode fiber, which can be further improved when all polarisation-spatial modes of the optical system are controlled.

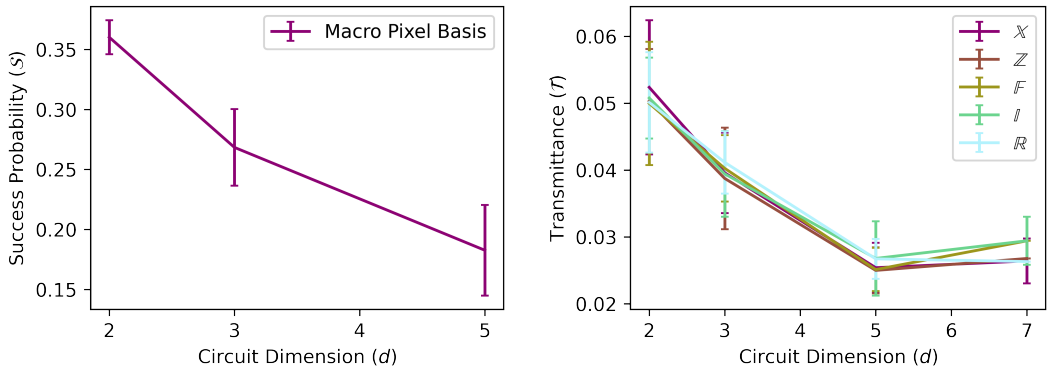

Figure S.3. Success probability (left) and optical transmittance (right) in macro-pixel input basis.

S.7. Manipulation of high-dimensional spatially entangled states

To study the programmabiltiy of our quantum circuits, we program many types of unitary gates, namely, identity-$\mathbb{I}$, Pauli-$\mathbb{Z}$, Pauli-$\mathbb{X}$, Fourier-$\mathbb{F}$, and random unitaries-$\mathbb{R}$, in $2, 3, 5$, and 7 dimensions in both the macro-pixel and OAM input bases. For each implementation, we randomly appoint a set of target output foci to encode the circuit with. We then use circuits to locally transform the d-dimensional spatially entangled two-photon state, which is then characterised by performing quantum state tomography.

Table. S.7 provides the average fidelities and purities of the reconstructed states for various types of gate and bases sampled over different sets of output foci. The histogram of fidelities of all the implemented gates are shown in Fig. S.7. Examples of the best-case measured tomography data and reconstructed density matrices of these manipulated states are shown in Fig. S.5 and Fig. S.6 for macro-pixel and OAM bases, respectively whose corresponding fidelities and purities are tabulated in Table. S.7.

Table S.2: Average fidelity $\mathcal{F}$ and purity $\mathcal{P}$ of output states ρ_o manipulated by a gate $\mathbb{T}$ in d dimensions in the macro-pixel and OAM bases. The standard deviation is calculated from an ensemble of implemented gates with different output foci, and for many realisations for the $\mathbb{R}$ gates.

Basis	$\mathbb{T}$	$\mathcal{F}(\rho, \rho_o)$				$\mathcal{P}(\rho_o)$			
		$d = 2$	$d = 3$	$d = 5$	$d = 7$	$d = 2$	$d = 3$	$d = 5$	$d = 7$
Macro-Pixel	$\mathbb{I}$	91.6 ± 4.7 %	87.9 ± 4.7 %	77.8 ± 5.2 %	70.2 %*	95.2 ± 1.4 %	96.0 ± 3.3 %	87.7 ± 2.9 %	73.3 %*
	$\mathbb{Z}$	92.1 ± 3.8 %	89.9 ± 3.8 %	73.7 ± 3.6 %	61.4 %*	95.5 ± 2.0 %	95.9 ± 2.0 %	87.8 ± 2.5 %	68.0 %*
	$\mathbb{X}$	91.7 ± 3.5 %	88.7 ± 4.0 %	73.3 ± 4.7 %	57.2 %*	95.3 ± 2.1 %	96.1 ± 2.7 %	86.6 ± 3.8 %	72.3 %*
	$\mathbb{F}$	89.1 ± 3.7 %	86.9 ± 2.0 %	69.9 ± 3.6 %	57.5 %*	88.9 ± 2.0 %	85.6 ± 1.8 %	78.4 ± 1.5 %	69.5 %*
	$\mathbb{R}$	89.4 ± 6.2 %	85.4 ± 2.7 %	73.2 ± 4.0 %	63.6 %*	92.3 ± 2.2 %	86.9 ± 1.5 %	80.8 ± 1.4 %	70.8 %*
OAM	$\mathbb{I}$	90.9 ± 2.2 %	86.7 ± 4.5 %	71.3 ± 3.7 %	60.3 ± 4.8 %	90.9 ± 0.4 %	82.2 ± 1.8 %	75.8 ± 1.9 %	68.9 ± 1.9 %
	$\mathbb{Z}$	91.6 ± 3.6 %	87.3 ± 2.9 %	73.8 ± 7.0 %	55.7 ± 9.3 %	90.1 ± 1.0 %	82.2 ± 1.1 %	76.0 ± 2.0 %	69.6 ± 1.5 %
	$\mathbb{X}$	94.1 ± 2.3 %	86.0 ± 4.1 %	74.3 ± 3.0 %	51.4 ± 6.5 %	92.6 ± 1.0 %	81.5 ± 2.3 %	76.5 ± 1.9 %	71.1 ± 2.8 %
	$\mathbb{F}$	91.0 ± 2.2 %	83.7 ± 4.4 %	70.7 ± 2.6 %	59.0 ± 5.8 %	92.2 ± 1.0 %	79.0 ± 1.4 %	75.5 ± 1.9 %	71.2 ± 0.7 %
	$\mathbb{R}$	91.2 ± 1.9 %	83.9 ± 3.0 %	72.4 ± 2.7 %	54.4 ± 6.7 %	91.0 ± 1.1 %	83.5 ± 4.7 %	76.3 ± 2.1 %	73.8 ± 0.9 %

*The standard deviation is not reported.

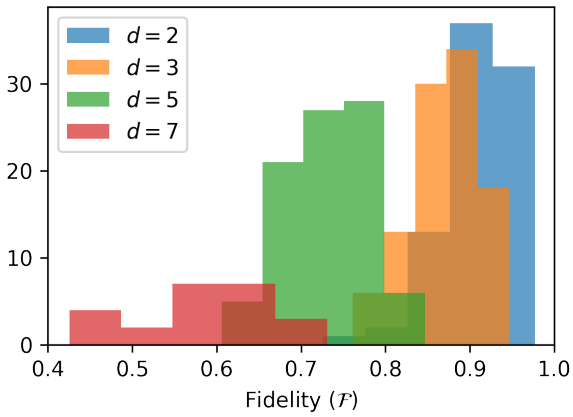

Figure S.4. Histogram of fidelities of optical circuits implemented in different dimensions

Table S.3: Fidelity $\mathcal{F}$ and purity $\mathcal{P}$ of output states ρ_o manipulated a gate $\mathbb{T}$ in d dimensions in the macro-pixel and OAM bases corresponding to the results presented in Fig. S.5 and S.6. The standard deviation is calculated using error propagation assuming Poisson statistics in photon counts.

Basis	$\mathbb{T}$	$\mathcal{F}(\rho, \rho_o)$				$\mathcal{P}(\rho_o)$			
		$d = 2$	$d = 3$	$d = 5$	$d = 7$	$d = 2$	$d = 3$	$d = 5$	$d = 7$
Macro-Pixel	$\mathbb{I}$	97.3 ± 0.3 %	94.4 ± 0.2 %	84.7 ± 0.4 %	73.1 ± 0.4 %	96.4 ± 0.8 %	97.8 ± 0.7 %	88.5 ± 0.9 %	70.3 ± 0.5 %
	$\mathbb{Z}$	97.7 ± 0.4 %	93.5 ± 0.3 %	77.7 ± 0.4 %	61.4 ± 0.4 %	97.9 ± 0.9 %	96.3 ± 0.9 %	90.3 ± 0.8 %	68.0 ± 0.6 %
	$\mathbb{X}$	97.1 ± 0.4 %	92.6 ± 0.2 %	78.8 ± 0.5 %	58.8 ± 0.5 %	96.5 ± 0.7 %	97.1 ± 0.7 %	91.3 ± 0.9 %	74.7 ± 0.4 %
	$\mathbb{F}$	96.0 ± 0.6 %	89.4 ± 0.4 %	75.9 ± 0.4 %	57.5 ± 0.4 %	92.2 ± 0.6 %	85.4 ± 0.7 %	80.4 ± 0.7 %	69.5 ± 0.5 %
	$\mathbb{R}$	96.5 ± 0.5 %	90.2 ± 0.2 %	81.1 ± 0.4 %	63.6 ± 0.4 %	92.9 ± 0.7 %	88.7 ± 0.5 %	83.1 ± 0.8 %	70.8 ± 0.6 %
OAM	$\mathbb{I}$	94.0 ± 0.1 %	94.6 ± 0.2 %	78.4 ± 0.3 %	65.7 ± 0.2 %	91.4 ± 0.3 %	81.5 ± 0.4 %	77.5 ± 0.4 %	70.8 ± 0.3 %
	$\mathbb{Z}$	94.3 ± 0.2 %	92.0 ± 0.1 %	81.2 ± 0.2 %	63.0 ± 0.2 %	89.2 ± 0.3 %	81.1 ± 0.3 %	78.5 ± 0.4 %	68.0 ± 0.3 %
	$\mathbb{X}$	96.8 ± 0.2 %	91.3 ± 0.2 %	77.5 ± 0.2 %	60.6 ± 0.2 %	92.4 ± 0.4 %	84.1 ± 0.3 %	79.1 ± 0.3 %	74.5 ± 0.3 %
	$\mathbb{F}$	93.8 ± 0.3 %	88.9 ± 0.3 %	75.5 ± 0.2 %	67.0 ± 0.2 %	93.5 ± 0.5 %	79.3 ± 0.4 %	77.5 ± 0.4 %	71.6 ± 0.3 %
	$\mathbb{R}$	93.0 ± 0.3 %	87.6 ± 0.2 %	75.4 ± 0.2 %	62.2 ± 0.2 %	91.6 ± 0.5 %	80.8 ± 0.3 %	76.8 ± 0.3 %	74.6 ± 0.3 %

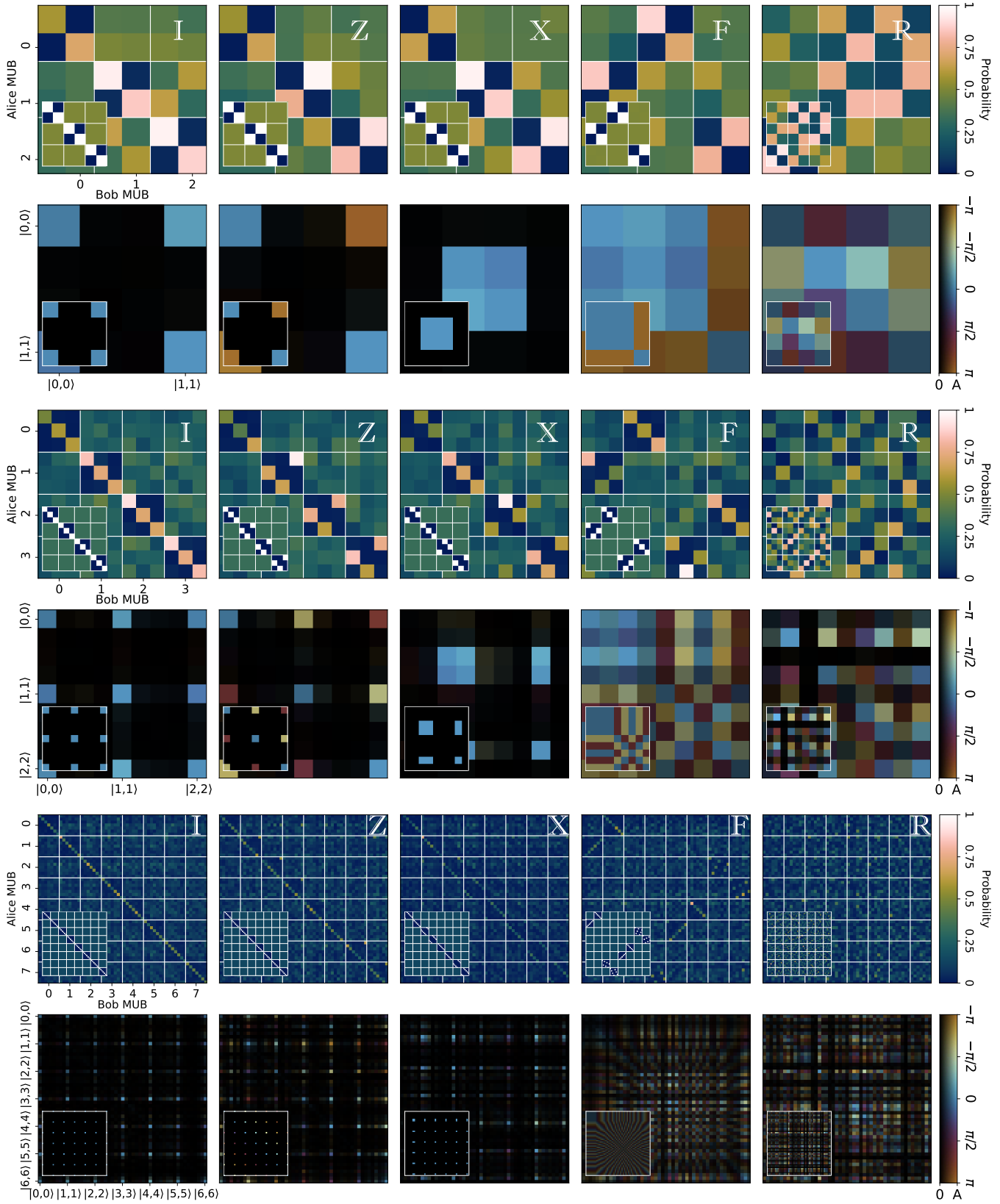

Figure S.5. Manipulation of 2, 3 and 7-dimensional spatially entangled two-photon states in the macro-pixel basis using the $\mathbb{I}$, Pauli-$\mathbb{Z}$, Pauli-$\mathbb{X}$, Fourier $\mathbb{F}$ and random unitary $\mathbb{R}$ gates. In each panel, the upper part shows the two-photon coincidence counts in all MUBs and the lower part depicts reconstructed density matrices.

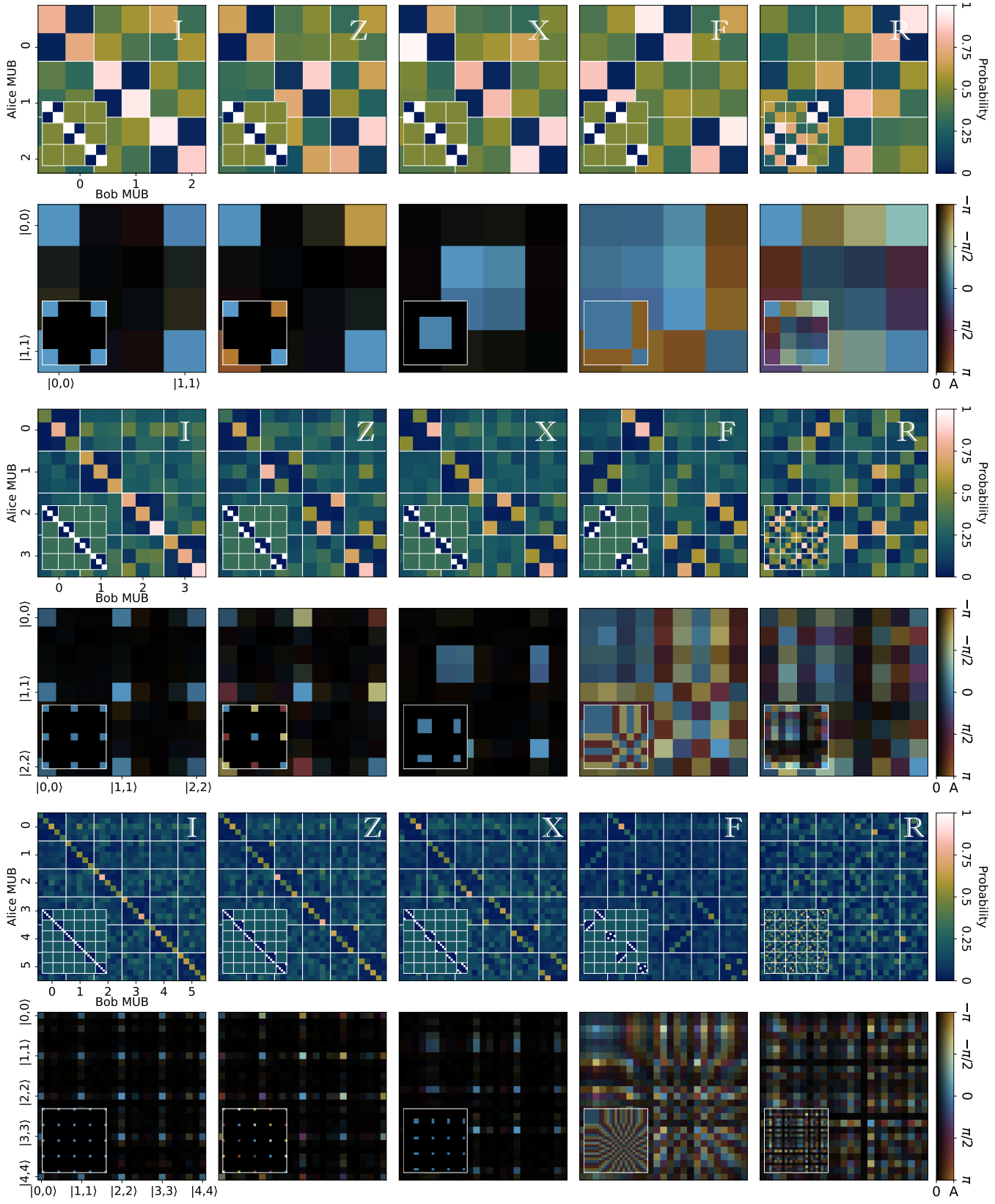
I
Z
X
F
R
Alice MUB
Bob MUB
Probability
|0,0⟩
|1,1⟩
|2,2⟩
|3,3⟩
|4,4⟩
A

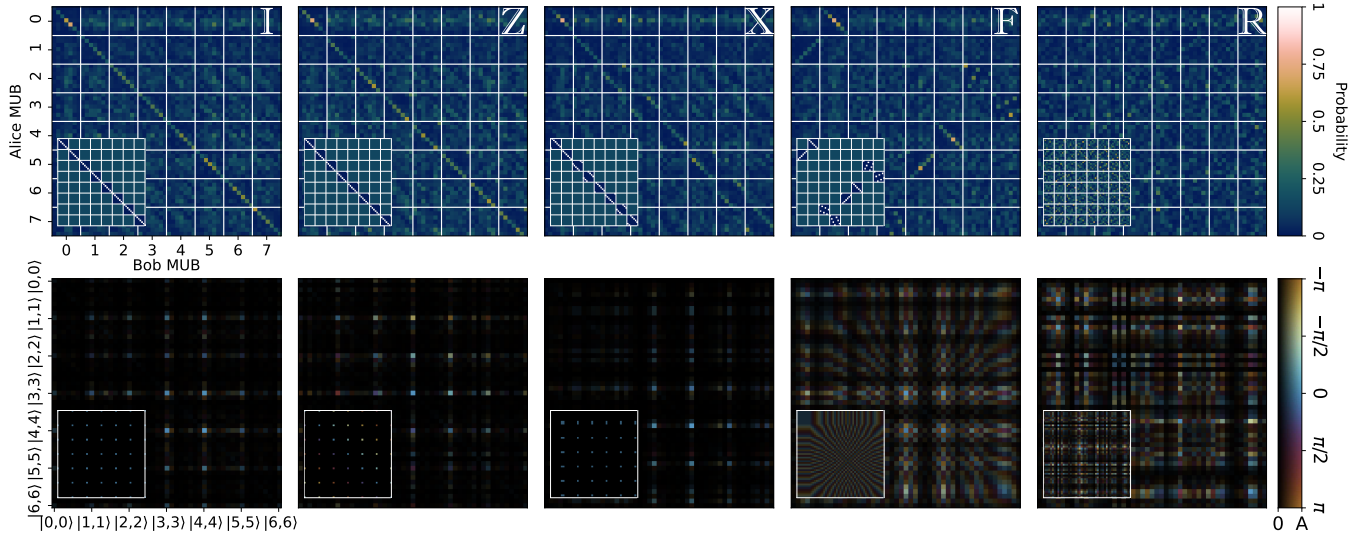

Figure S.6. Manipulation of 2, 3, 5 and 7-dimensional spatially entangled two-photon states in the OAM basis using the $\mathbb{I}$, Pauli-$\mathbb{Z}$, Pauli-$\mathbb{X}$, Fourier $\mathbb{F}$ and random unitary $\mathbb{R}$ gates. In each panel, the upper part shows the two-photon coincidence counts in all MUBs and the lower part depicts reconstructed density matrices.

S.8. Programmability and scalability of top-down designed circuits

To investigate the programmability and scalability of our approach, we numerically construct many instances of the high-dimensional circuits by varying our design parameters, i.e., dimension of circuit n, dimension of mode mixers d, depth of circuit L, using the model

$$\mathbf{T} \coloneqq U_{L+1} \prod_{j=1}^{L} P_j U_j, \tag{S.8.1}$$

where the n reconfigurable phase elements at each P_j are found using the wavefront-matching algorithm as explained in S.5 given a set of $n \times n$ unitary matrices $\{U_j\}_j$ and a set of d input and output modes of interest. The codes for these simulations are available in [83]. Once a circuit is implemented, we classify its performance by measuring fidelity (Eq. S.6.2) and success probability (Eq. S.6.3). For a given set of design parameters n, L and d, we implement at least 100 realisations of the Identity $\mathbb{I}$, Pauli-$\mathbb{X}$, Pauli-$\mathbb{Z}$, Fourier-$\mathbb{F}$, and random unitary $\mathbb{R}$ gates (Eq. S.5.4), by varying the set of d input and output modes of interest which can be randomly selected or specifically assigned. We simulate these circuits by treating the mode-mixers $\{U_j\}_j$ as either a set of random unitaries, or discrete Fourier transforms (DFT).

As presented in the main text, when the dimension of the circuit d is less than the dimension of mode mixers n ($d/n < 0.1$), both fidelity and success probability reduce as the circuit dimension, d, increases. Fig. S.7 conveys these trends in detail. For all these realisations, all mode mixers $\{U_j\}$ correspond to the same random unitary matrix, and the positions of input/output modes of interest are randomly selected for each implementation. The behaviour reported in Fig. S.7 is also observed either when different random mode-mixers are used in each layer, or input/output modes are specifically assigned to the first d modes of the U_j.

For a device described by Eq. S.8.1, the total number of degrees of freedom is given by the number of reconfigurable elements nL. On the other hand, the constraints to program a d-dimensional circuit $\mathbb{T}$ is $\mathcal{O}(d^2)$ [6, 84]. A larger d leads to loss of performance because the number of constraints required to program the circuit increases. Thus, as d increases, the number of reconfigurable elements does not change. Improving the figures of merit of a d-dimensional circuit can therefore be addressed in two primary ways: increasing the dimension of mode mixers, n, or the depth of circuit, L. As shown in Fig.S.8a, the fidelity will rise to unity when the total number of reconfigurable elements exceeds the number required to program a unitary operation ($\mathcal{O}(d^2)$). The point at which $\mathcal{F} = 1$ depends on the ratio of d/n. In the case where $d = n$, the number of reconfigurable elements required is optimal, whereas in the cases where $d/n < 1$, the number of reconfigurable elements necessary for the full programmability increases as d/n decreases.

With respect to the success probability, we observe that it increases as a function of the circuit depth and reaches unity when $L \approx \mathcal{O}(d)$ in all cases of $d \leq n$ (Fig.S.8b). In this regime, full programmability is achieved and is seen to be independent of d/n.

These results imply that in order to achieve both high fidelity and success probability, one does not need to solely rely on the number of reconfigurable elements, but also on their distribution across the circuit. Ideally, one would want to implement a fully programmable circuit using the full dimension of mode mixers ($d = n$) constructed from 2×2 beam splitters or $n \times n$ mode mixers, since this achieves the minimum number of reconfigurable elements [5, 7]. However, it is known that in the presence of imperfections, an increase in the depth of the circuit is required to improve the fidelity in such schemes [13–15]. Scaling the depth of circuit in practice may nonetheless not be the most viable option due to a variety of experimental reasons, namely, propagation and interface losses and accumulation of errors. Instead of considering errors and scattering losses as a problem, the top-down approach presents a reasonable alternative ($d < n$ and $L \lesssim \mathcal{O}(d)$) where randomness is exploited to implement a circuit with a low depth. Here, both fidelity and success probability are acceptably high while n can increase to improve the fidelity without reducing the success probability from unity when $L > 2d$, or with a trade-off on the success probability when $L \leq 2d$. Many optical devices, for instance, computer-generated holograms and MPLC device [22, 85], can be considered to be in this category where mode-mixing can be implemented by free-space propagation, a $2f$ lens system, or another transformation such as a circulant matrix [86, 87].

Finally, while the deterministic construction of programmable circuits from discrete Fourier transforms is known for $d = n$ [88, 89], a proof of universal programmability of unitary circuits using random-unitary mode mixers remains open to the best of our knowledge, and the deterministic construction of such circuits is yet to be discovered.

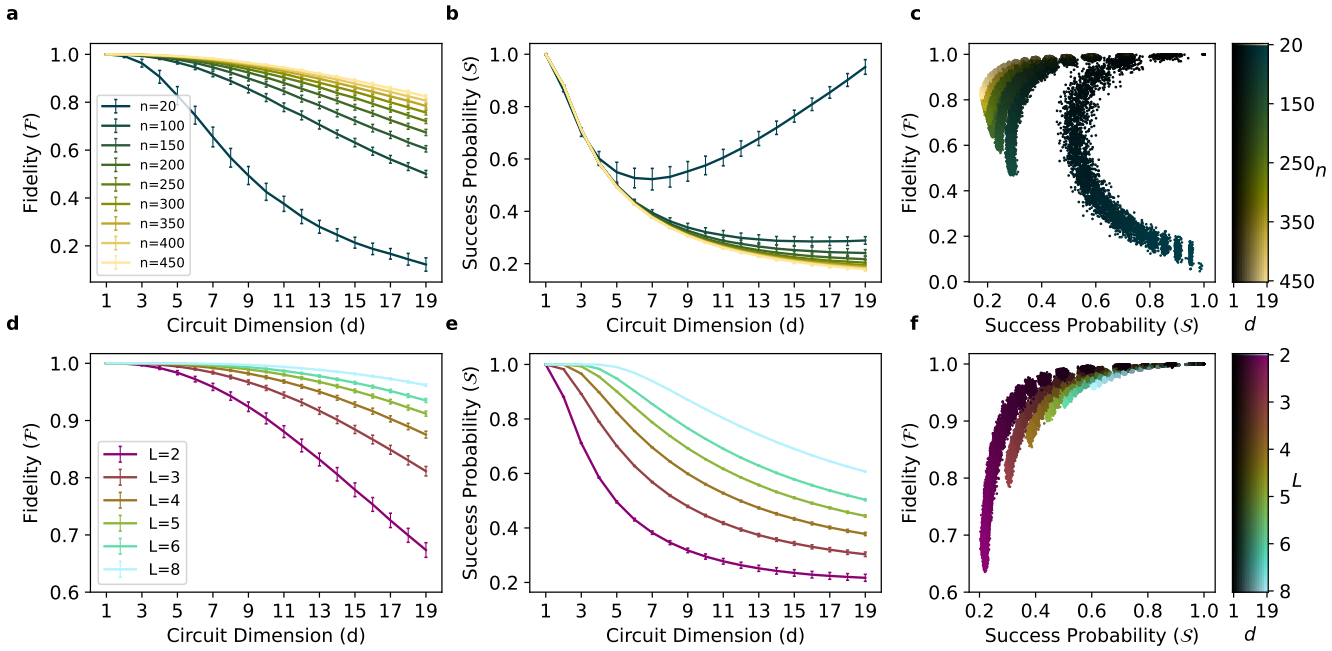

Figure S.7. **Simulated fidelity $\mathcal{F}$ and success probability $\mathcal{S}$ for all gates implemented in a circuit with random unitary mode mixers**: (a-c) $\mathcal{F}$ and $\mathcal{S}$ as a function of the dimension of mode-mixers, n, with a circuit depth $L = 2$ and (d-f) $\mathcal{F}$ and $\mathcal{S}$ as function of circuit depth L while using mode-mixers with dimension $n = 200$.

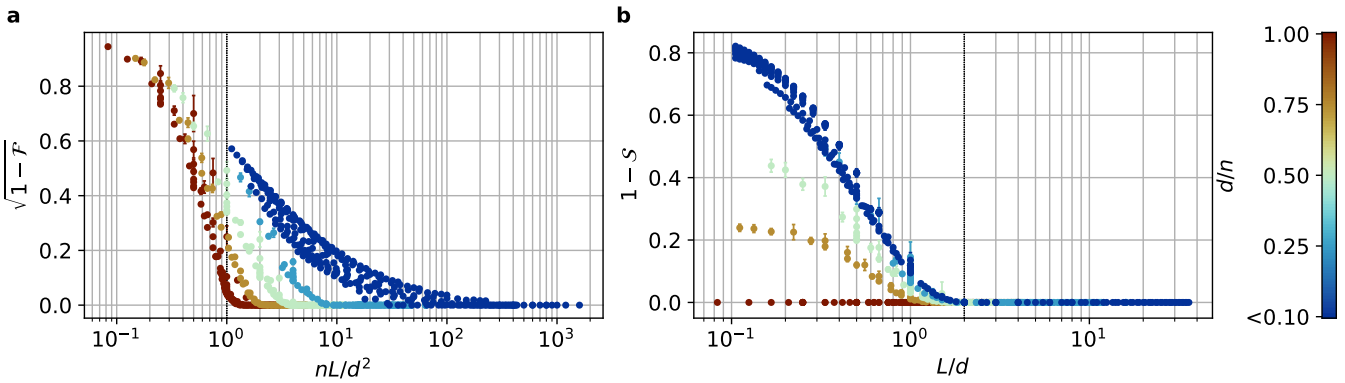

Figure S.8. Upper bound of trace distance $\sqrt{1-\mathcal{F}}$ (a) and success probability $\mathcal{S}$ (b) for all simulated gates implemented in a circuit with random-unitary mode-mixers.